Toyama Daigaku Kenkyusuisinkikou Suiso Doitai Kagaku Kenkyu Senta Kenkyu Hokoku
ISSN 1346-3675

Annual Report of Hydrogen Isotope Research Center,
Organization for Promotion of Research,
University of Toyama, JAPAN
VOL 36 2016

富山大学研究推進機構水素同位体科学研究センター

研　究　報　告

第 36 巻

2016

富山大学研究推進機構 水素同位体科学研究センター

HYDROGEN ISOTOPE RESEARCH CENTER,

ORGANIZATION FOR PROMOTION OF RESEARCH, UNIVERSITY OF TOYAMA

目　次

総　説

不均一系光触媒反応における光生成電荷の分離機構 …… 萩原英久 …… 1

論　文

光電子増倍管の印加電圧を制御する改良積分法の液体シンチレーション計測への応用 …… 原正憲、坂口春菜、中山将人、阿蘇司、庄司美樹、古澤孝良、加藤結花、吉村共之 …… 21

Pd–Ag–Rh 三元系合金における磁化率と水素吸収量の相関 …… 赤丸悟士、原正憲 …… 31

多角バレルスパッタリング法を用いて調製した Ru–Ni/TiO_2 触媒の CO_2 メタン化反応特性 …… 井上光浩、島明日香、宮崎かほり、専光寺旭洋、ｵﾏｰﾙ ﾒﾝﾄﾞｰｻ、魯保旺、曽根理嗣、阿部孝之 …… 39

ノート

α-Al_2O_3 担持 Pt ナノ粒子触媒の CO 酸化活性と着火現象 …… 田口明、尾崎智弘 …… 45

I N D E X

Review

H. HAGIWARA
Separation Mechanism for Photogenerated Charge Carriers in Heterogeneous Photocatalysts 1

Original

M. HARA, H. SAKAGUCHI, M. NAKAYAMA, T. ASO, M. SHOJI, T. FURUSAWA, Y. KATO, T. YOSHIMURA
Modified integral counting method by controlling high voltage of photomultipliers for liquid scintillation counting 21

S. AKAMARU, M. HARA
Relation between the magnetic susceptibility and the amount of absorbed hydrogen for the Pd–Ag–Rh ternary alloy 31

M. INOUE, A. SHIMA, K. MIYAZAKI, T. SENKOJI, O. MENDPZA, B. LU, Y. SONE, T. ABE
CO_2 Methanation Performance of a Ru–Ni/TiO_2 Catalyst Prepared by the Polygonal Barrel-Sputtering Method 39

Note

A. TAGUCHI, T. OZAKI
Ignition-extinction phenomena in CO oxidation reaction over “dry” impregnated platinum nanoparticles on α-Al_2O_3 45

富山大学研究推進機構水素同位体科学研究センター研究報告 36：1－19，2016.

総　説

不均一系光触媒反応における光生成電荷の分離機構

萩原　英久

富山大学　研究推進機構　水素同位体科学研究センター
〒930-8555 富山市五福 3190

Separation Mechanism for Photogenerated Charge Carriers in Heterogeneous Photocatalysts

Hidehisa Hagiwara

Hydrogen Isotope Research Center, Organization for Promotion of Research,
University of Toyama, Gofuku 3190, Toyama, 930-8555, Japan

(Received June 30, 2017; accepted July 31, 2017)

Abstract

In heterogeneous photocatalysts, it is very important to move photoexcited charges in the semiconductor to the reaction site on the surface without recombination. In this review, we describe the process of the photocatalytic reaction from photoexcitation of semiconductor photocatalyst to surface redox reaction, and summarized various researches on the charge separation of photogenerated electrons and holes in semiconductors reported up to the present.

1. Introduction

Heterogeneous photocatalysts have been widely used for various applications such as antibacterial coating,[1,2] deodorizing,[3] antifogging treatment,[4,5] and water purification,[6,7] and become more important in the future. Furthermore, a photocatalytic solar energy conversion,

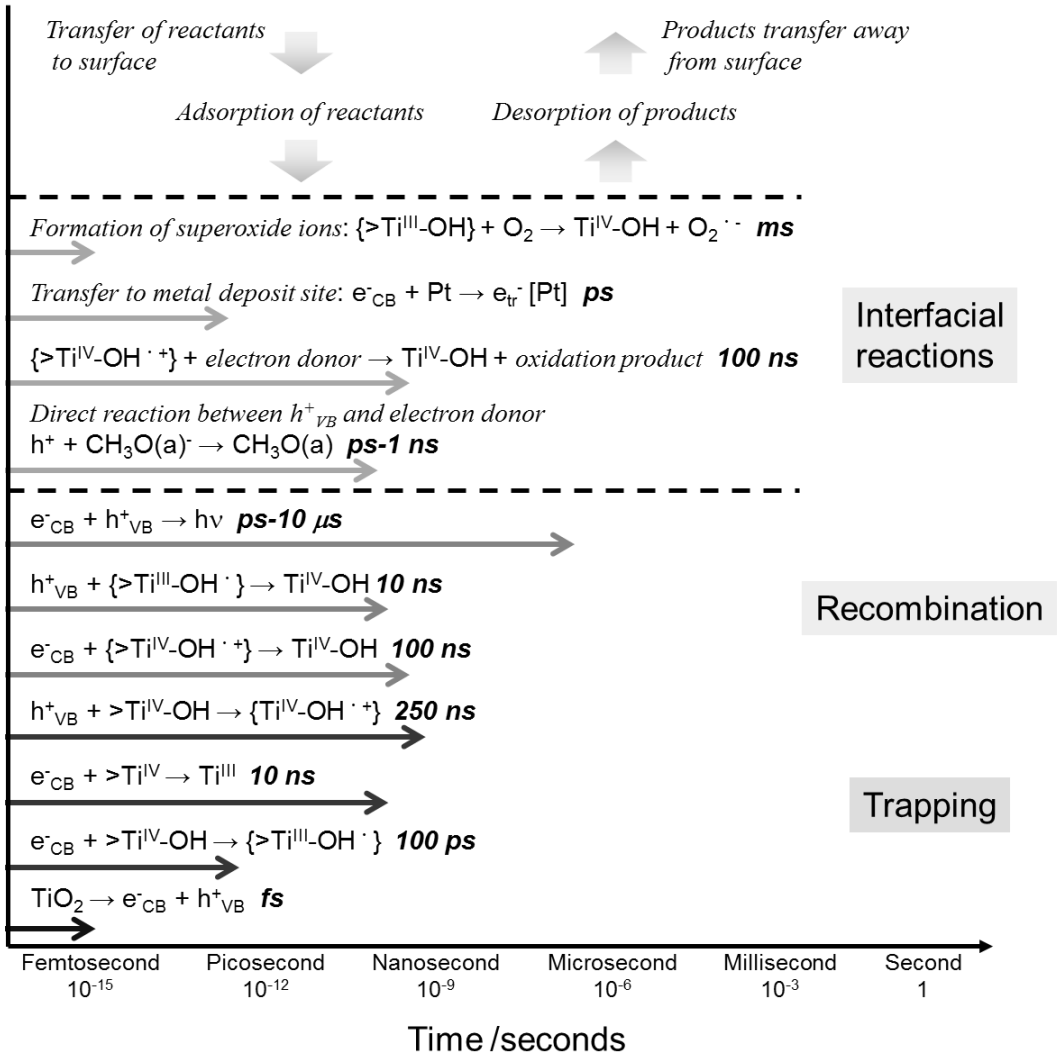

Fig. 1 Elementary reactions in TiO_2 photocatalysis with corresponding timescales.

so-called artificial photosynthesis, has actively studied to solve global energy problems.[8,9] To improve the activity and the functionality of photocatalysts, it is necessary to understand a series of photocatalytic processes in detail. Figure 1 shows elementary reactions of TiO_2 photocatalyst with corresponding timescales. Under light irradiation with a higher energy than the bandgap energy of the semiconductor photocatalyst, electrons in the valence band (VB) make transition to the conduction band (CB) with leaving holes in the valence band. While the photogenerated electrons transfer to the bottom of the CB, the holes transfer to the top of the VB, via vibrational relaxation process. These charge generation and relaxation processes occur in the order of

femtoseconds. The photogenerated electrons and holes diffuse in the CB and the VB, respectively, and part of them are trapped at the energy level formed by atomic vacancy, impurity, or functional groups on the photocatalyst surface. In the charge recombination process, the photogenerated charge carriers annihilate each other releasing the energy as a photon or phonons. These trapping and recombination processes take place in the order of nanoseconds or microseconds. On the other hand, the photogenerated electrons and holes without recombination react with adsorbed chemical species, or transfer to metal or metal oxides on the photocatalyst surface. The redox reactions on the photocatalyst surface occur in the order of the microseconds or milliseconds, thus it is considered that the photocatalytic activity is improved by suppressing the charge recombination at trap site or photocatalyst surface. Therefore, this review covered up the several approaches of the photogenerated carrier separation in heterogeneous photocatalysts, for development of the highly active photocatalysts.

2. Charge separation in semiconductor photocatalysts

Photogenerated electrons and holes in optical semiconductors diffuse in conduction and valence bands along electric fields. In silicon type solar cells, the charge separation takes place at the interface between p-type semiconductors (e.g. boron-doped silicon) and n-type

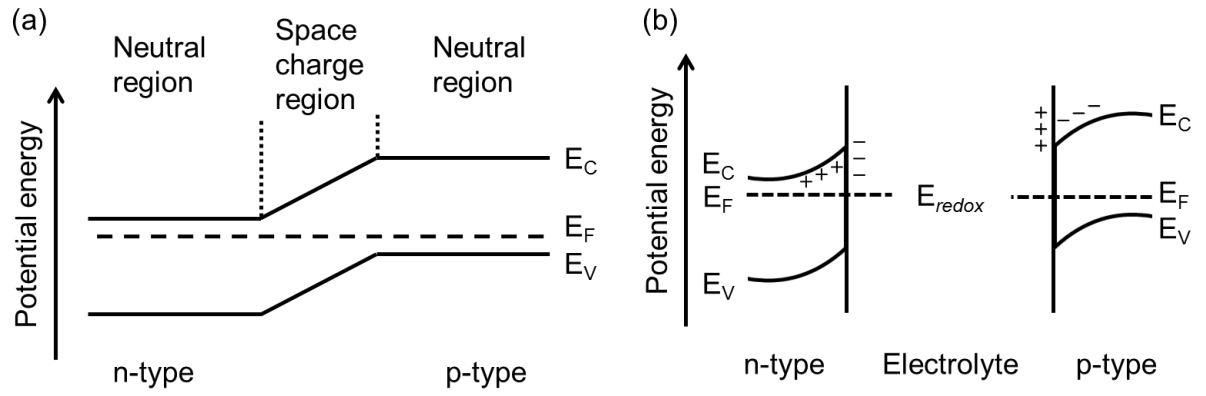

Fig. 2 Energy band diagrams of (a) p-n junction and (b) semiconductor-electrolyte interface.

semiconductors (e.g. phosphorus-doped silicon), so-called p-n junction, because of a potential gradient in a space charge region (Fig. 2a). The formation of space charge region in semiconductor photoelectrodes of photoelectrochemical cells are explained by a band-bending model, which is based on an interdiffusion of electrons and holes between semiconductors and redox species in electrolyte (Fig. 2b). In the case of semiconductor photocatalyst powders, the space charge region forms in a similar manner to that of the photoelectrodes. The length of the space charge region depends on the carrier density of the semiconductor photocatalysts, and it is estimated within 20-100 nm.[4,10] Therefore, the reduced effect of the band bending is one of the reasons for increasing charge recombination in photocatalyst particles with size within 100 nm. Although the space charge properties are determined by surface/interface electronic states, the photogenerated charges can also be controlled by electric fields induced dielectric structures or difference in the surface electronic band structures of crystal facets, as described below.

2.1. Ferroelectric materials

Barium titanate ($BaTiO_3$), which is one of the most popular ferroelectric materials, has been investigated to reveal the charge separation effect of internal electric fields.[11-17] $BaTiO_3$ shows the spontaneous polarization between 278 K and 393 K, because Ti and Ba atoms shifted to <100> direction and O atoms shifted negatively from cubic perovskite structure, as shown in Fig.3.[18] To confirm the effect of the spontaneous polarization on the charge separation and the photocatalytic reactivity, Ag^+, Pb^{2+}, and Mn^{2+} ions were employed as reaction marker. These ions were deposited on the photocatalyst surface as Ag, PbO_2, and MnO_2 by photocatalytic reduction or oxidation reactions, and the migration behavior of

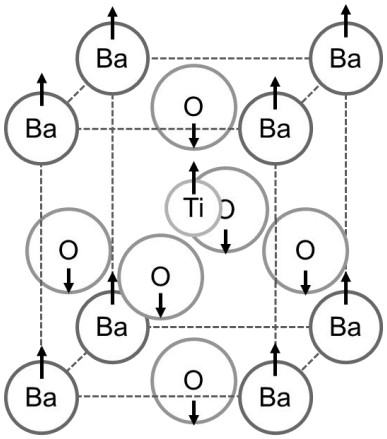

Fig. 3 Crystal structure of $BaTiO_3$.

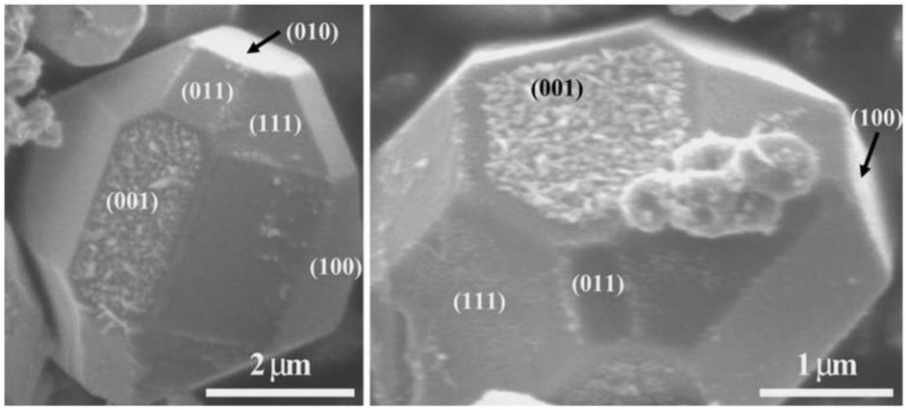

Fig. 4 SEM images of faceted $BaTiO_3$ crystals after reaction in $AgNO_3$ aqueous solution Reproduced with permission from Ref. 17, copyright Springer Science+Business Media, LLC 2008.

photogenerated carriers in semiconductor crystals was determined by surface observation. Figure 4 shows SEM images of $BaTiO_3$ crystals prepared after the photoirradiation in $AgNO_3$ aqueous solution.[17] In this study, $BaTiO_3$ crystals were prepared by KCl flux method, and the deposition of Ag particles was observed on (001) plane of $BaTiO_3$ crystals. This result suggests that Ag is reduced by photogenerated electrons migrated along the direction of ferroelectric polarization. In addition to the research on $BaTiO_3$, various ferroelectric materials, such as $Pb(Zr, Ti)O_3$,[19-26] $BiFeO_3$,[27] $LiNbO_3$,[28] and $Sr_2Nb_2O_7$,[17] have been reported as active photocatalysts for water splitting, hydrogen production, and water purification.

The photocatalytic properties of pyroelectric materials have been also studied for understanding the efficient charge separation. Huang et al. reported that bismuth-based compounds, $BiOIO_3$,[29] $Bi_2O_2[BO_2(OH)]$,[30] and $Bi_4V_2O_{11}$[31] showed high photocatalytic activity for organic compound oxidation or oxygen formation from $AgNO_3$ aqueous solution. As shown in Fig. 5, $BiOIO_3$ is composed of central Bi_2O_4 layer shares O corners with IO_3 units, thus the direction of the pyroelectric polarization is along *c*-axis. The DFT calculations of $BiOIO_3$ revealed that Bi 6p and I 5p contributes to the CB while O 2p strongly contributes to the VB. Therefore, the photoexcited electrons in the CV migrate to Bi_2O_4 layer along *c*-axis, and the

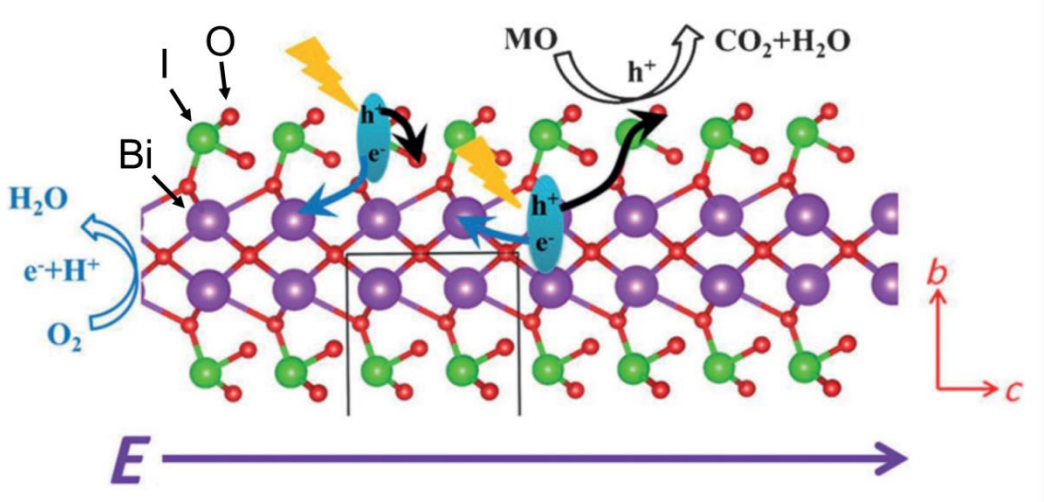

Fig. 5 A perspective view of the $BiOIO_3$ slab. Reproduced with permission from Ref. 29, copyright (2013) Wiley-VCH Verlag GmbH & Co. KGaA, Weinheim.

photogenerated holes located at the O 2p. This charge separation process is important for the photocatalytic property of bismuth-based photocatalysts. Related study of the pyroelectric polarization effect on the photogenerated charge separation in bismuth-based oxyhalides, such as carbon-doped Bi_3O_4Cl,[32] $Bi_{12}O_{17}Cl_2$,[33] and BiO_X (X=Cl, Br, I),[34-36] have been also reported from different research groups. Furthermore, Huang et al., also reported silver silicates, $Ag_6Si_2O_7$,[37] $Ag_9(SiO_4)_2NO_3$,[38] $Ag_{10}Si_4O_{13}$,[39,40] as the pyroelectric photocatalysts. As described above, the internal polar electric fields in semiconductor photocatalyst enhance the charge separation of the photogenerated carriers and improve the photocatalytic activity.

2.2. Crystal facets

The surface electronic band structures depend on surface facets because of the surface atomic arrangements and adsorption species. Redox abilities of photogenerated charge carriers tuned by the surface electronic band structures of different facets, and accumulations of photogenerated electrons or holes on different facets.[41] Ye et al. reported the photoinduced

charge transfer properties of anatase TiO_2 crystal between (101) facets and (001) facets.[42] They prepared TiO_2 crystals by using a hydrothermal synthesis method with ammonium hexafluorotitanate ($(NH_4)_2TiF_6$), tetrabutyl titanate, and hydrochloric acid (HCl), and controlled the ratio of different facets by changing the hydrothermal temperature and the volume ratio of HCl and water. As shown in Fig. 6, the photogenerated electrons and holes efficiently separated to (101) facet and (001) facet, and thus reduction and oxidation reactions took place on each facet. The spatial charge separation between different facets of TiO_2 crystal, containing other crystal structure, brookite[43] and rutile,[44] has been reported by several research groups.[45-51] To date, the effect of spatial charge separation between different facets on the photocatalytic reactivity have been studied by using various photocatalytic semiconductors, such as metal oxides (CeO_2[52] and Cu_2O[53-55]), complex oxides ($BiVO_4$,[41,56-58] $SrTiO_3$,[59,60] $La_2Ti_2O_7$,[61] and $BaLa_4Ti_4O_{15}$[62,63]), metal oxyhalides,[64-66] and metal sulfides.[67,68]

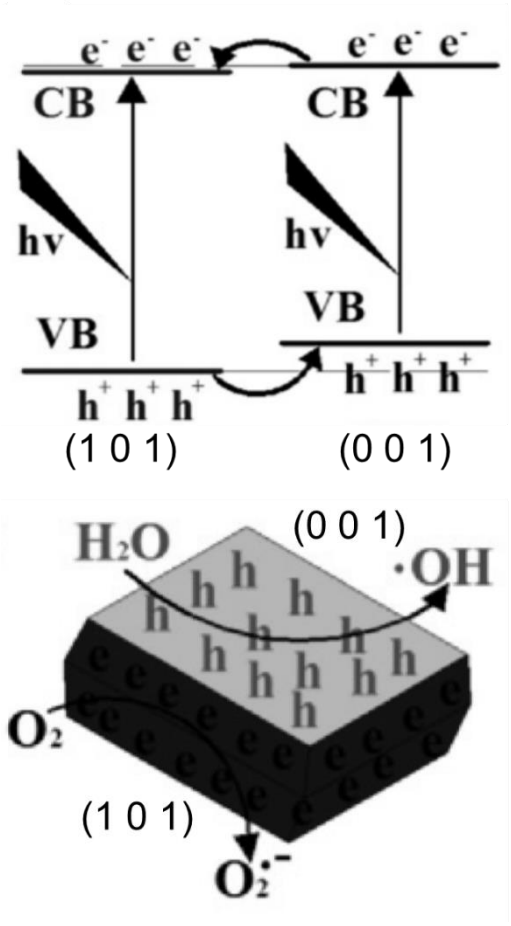

Fig. 6 Electronic band structures and charge distribution of (101)-(001) facets. Reproduced with permission from Ref. 42, copyright (2013) Elsevier.

3. Charge trapping

Diffusion and trapping of the photogenerated carriers after the charge separation is also important factor for the activity of photocatalyst materials. In addition to the conduction and

valence band levels, there are several energy levels in semiconductors, as shown in Fig. 7. The depth of the charge trap levels depends on how the defects stabilize the trapped charges through polaron formation.[69-71] To understand the relationship between the trap sites and the photocatalytic activity, time-resolved photoabsorption spectroscopy is generally employed for the lifetime measurement of the photogenerated electrons and holes.[72-75] Yamakata et al. reported that the photocatalytic activity of $SrTiO_3$ was improved by $SrCl_2$ flux treatment because of the prolongation of photogenerated charge lifetime with decreasing the number of deep trap sites.[76] They also investigated the relationship between the surface defects and the photocatalytic activity by using single- and poly- crystals of $SrTiO_3$.[77] Although the free and shallow trapped electrons were dominant in single crystal $SrTiO_3$, they recombined within 50 ns. On the other hand, defect-rich polycrystalline $SrTiO_3$ showed the long-time charge separation longer than 1 ms and the higher photocatalytic activity for hydrogen production from methanol aqueous solution. This positive effect of surface defects on the photocatalytic activity have been reported by using other semiconductor materials. Hoch et al. reported that the activity of photocatalytic CO_2 reduction on $In_2O_{3-x}(OH)_y$ strongly enhanced by introducing surface defects as oxygen vacancies and hydroxyl groups.[78] Furthermore, the positive effect of surface vacancy has been reported on the photodecomposition activity of BiOCl for organic compounds.[79] Whereas the deep trap sites in semiconductors work as recombination center of photogenerated charges, the surface defects prolonged charge separation lifetime and enhanced the photocatalytic activity.

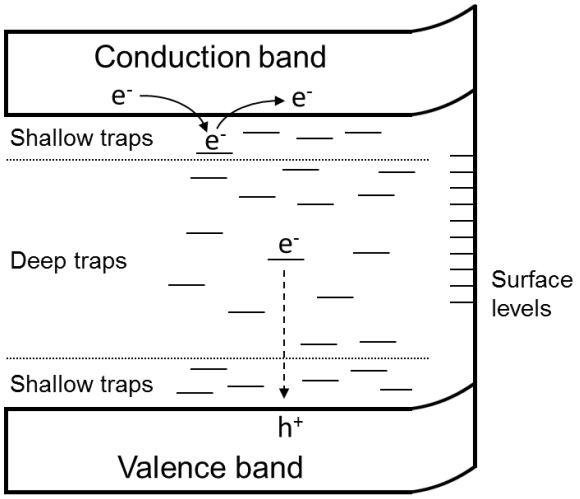

Fig. 7 Schematic image of electronic band structure of a semiconductor with various energy levels.

These results are important for the design of highly active photocatalysts.

4. Interfacial charge transfer

In multi-component photocatalysts, junctions are formed through the combination of a semiconductor with other materials to enhance charge separation. In this section, the topics of semiconductor-semiconductor, semiconductor-metal complex, and semiconductor-metal (or metal oxide) co-catalyst photocatalysts are introduced.

4.1. Semiconductor-semiconductor heterojunction

Until now, various photocatalysts with semiconductor junction have been developed, and mainly used TiO_2-based composites (e.g. Fe_2O_3,[80-85] Cu_2O,[86-89] ZnO,[90,91] WO_3,[92,93] Ag_3PO_4,[94,95] In_2O_3,[96-99] CeO_2.[100-102] Furthermore, semiconductor composites with different crystal phase were investigated, especially anatase-rutile TiO_2 composites.[103-105] Wang et al. reported the composite effect of α-Ga_2O_3 and β-Ga_2O_3 on the photocatalytic water splitting activity.[106] The

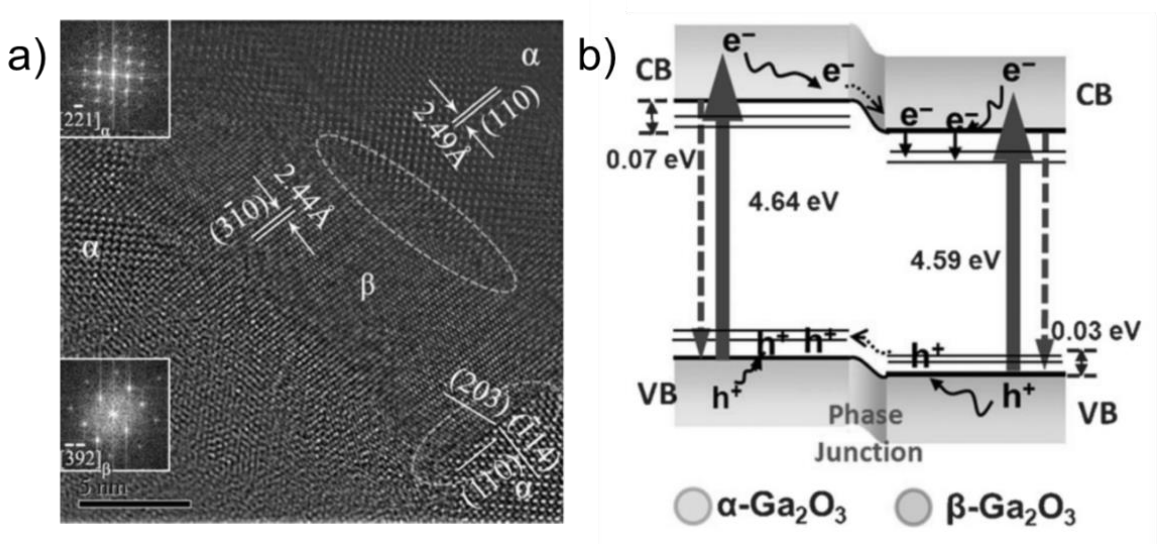

Fig. 8 (a) HR-TEM image of Ga_2O_3 calcined at 863 K. (b) Illustration of charge transfer cross the a–b phase junction. Reproduced with permission from Ref. 106, copyright (2012) Wiley-VCH Verlag GmbH & Co. KGaA, Weinheim.

composite of α-Ga_2O_3 and β-Ga_2O_3 was prepared by adjusting calcination temperature, and effective charge separation was achieved at well-developed phase junction (Fig. 8). A similar effect was observed in the composite of α-Bi_2O_3 and β-Bi_2O_3.[107] In this system, the photogenerated electrons moved to the CB of β-Bi_2O_3 and holes moved to the VB of α-Bi_2O_3. The photocatalytic activity for organic dye decomposition was improved by the formation of heterojunction. In recent years, composite photocatalysts of inorganic semiconductors and metal sulfides,[108-113] metal halides[114-116] and organic semiconductors[117,118] have also been reported in addition to metal oxides. The formation of heterojunction at semiconductor interface is one of the effective way to separate photogenerated charges in photocatalysts.

4.2. Semiconductor-metal complex heterojunction

The effects of surface modification with metal complexes for semiconductor materials were investigated in the research area of photoelectrochemical cells, and dye-sensitized solar cells are one of the typical research. In the dye-sensitized system, photo-excited electrons in dyes inject to the CB of metal oxide semiconductors along the potential gradient formed by band-bending, and the photogenerated charges are effectively separated spatially between metal oxides and dye molecules (Fig. 9). Most of dye-sensitized photocatalyst systems have been fabricated using TiO_2 and metal complexes, such as ruthenium complexes[119-121] and porphyrins.[122-125] Hirano et al. studied the ligand effects of Ru-complexes on the photocatalytic activity of dye-sensitized Pt/TiO_2 for hydrogen production

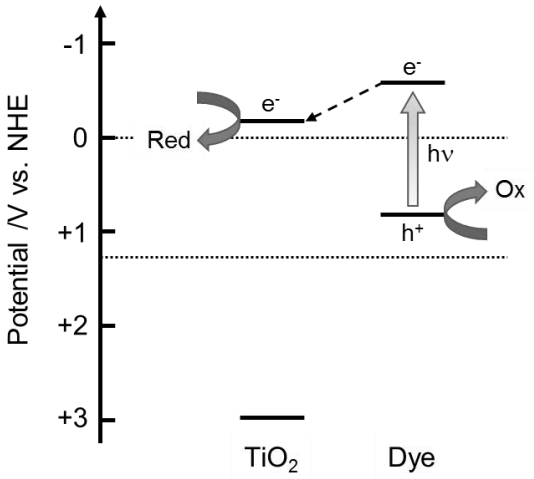

Fig. 9 Schematic image of charge transfer mechanism of dye-sensitized photocatalysts.

from EDTA aqueous solution.[120] They used $Ru(bpy)_3^{2+}$, $Ru(dcbpy)_3^{4-}$, and $Ru(bpym)_3^{2+}$ as sensitization dye, and $Ru(bpym)_3^{2+}$-Pt/TiO_2 showed the highest photocatalytic activity. $Ru(bpym)_3^{2+}$ contains more nitrogen in the molecular structure, which showed higher affinity with the TiO_2 surface than other Ru-complexes, resulted in enhanced electron transfer to TiO_2. The same tendency was reported in various Ru-complexes,[126-128] thus the strong affinity between metal oxides and dyes are important for the charge separation and the photocatalytic activity of the dye-sensitized photocatalysts.

On the other hand, the electron injection from the CB of semiconductor to metal complex molecules also reported for the dye-semiconductor composite photocatalysts. We developed chromium tetraphenylporphyrin chloride/Zr-doped $KTaO_3$ (Cr-TPPCl/$KTa(Zr)O_3$) composite photocatalysts for water splitting reaction.[129-131] In this system, the water splitting takes place with two-step excitation process in both semiconductors and dyes, as shown in Fig. 10. This charge transfer mechanism is similar to that of light-dependent reaction of photosynthesis, so-called Z-scheme. The half-life of the charge separation lifetime of $KTa(Zr)O_3$ was prolonged

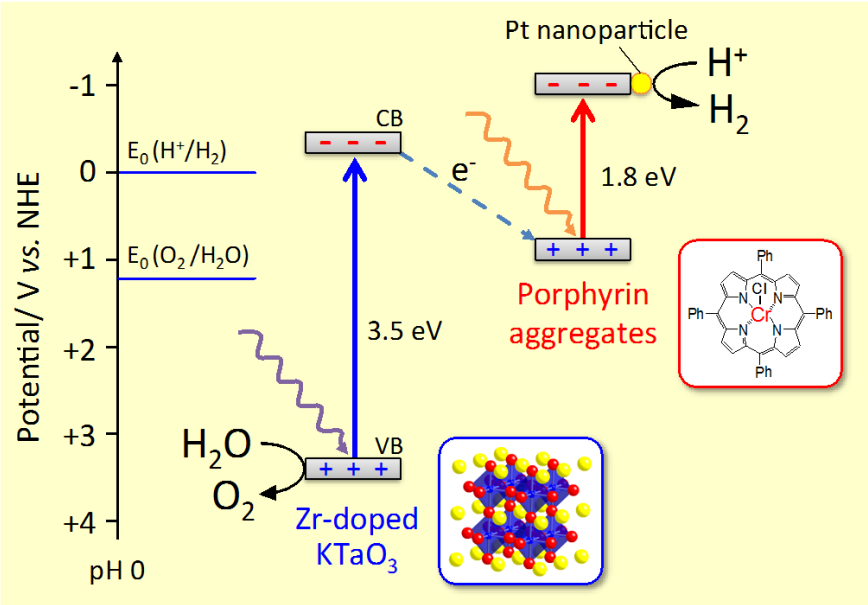

Fig. 10 Schematic image of charge transfer mechanism of Cr-TPPCl /$KTa(Zr)O_3$ composite photocatalyst.

from 11.5 μs to 100 μs by Cr-TPPCl modification, and thus the photocatalytic activity was improved.[129] Sekizawa et al. also reported Ag/TaON-Ru binuclear complex as Z-scheme type photocatalyst for photocatalytic CO_2 fixation.[132] Although the Z-scheme photocatalysts need two photons for the photocatalytic reaction, efficient charge separation can be achieved.

4.3. Semiconductor-metal (metal oxide) co-catalysts

The co-catalysts act as acceptors of the photogenerated carriers for separating the electrons and the holes from the CB and the VB of the semiconductor, and as more efficient active sites for the photocatalytic reaction. The most commonly used metals for co-catalysts are platinum (Pt), rhodium (Rh), or palladium (Pd) nanoparticles due to their noble and catalytic properties.[133–135] Besides noble metal nanoparticle, metal oxide (NiO, RuO_2), metal sulfides,

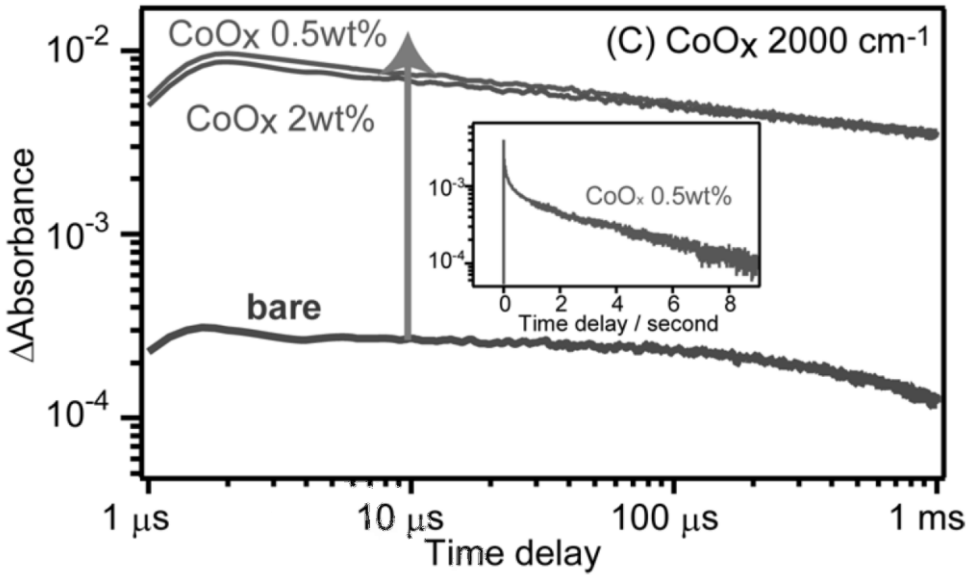

Fig. 11 Decay of transient absorption of CoO_x-loaded $LaTiO_2N$ photocatalysts in a vacuum. The transient absorption was measured at 2000 cm^{-1}. The sample was excited by 355 nm UV laser pulses (6 ns duration, 0.5 mJ cm−2, 1 Hz). The inset shows the decay in the second region (pump pulse repetition rate at 0.01 Hz). Reproduced with permission from Ref. 143, copyright (2014) American Chemical Society.

and CoPi have been investigated as co-catalysts.[136-142] Yamakata et al. investigated the loading effect of Pt and CoO_X co-catalysts on $LaTiO_2N$ by using time-resolved absorption spectroscopy.[143] In the case of $LaTiO_2N$, photogenerated holes in the VB of $LaTiO_2$ were captured rapidly by CoO_X in a few picoseconds, and the lifetime of electrons were prolonged to the second region (Fig. 11). Loading co-catalysts enhance the charge separation of semiconductor photocatalysts and decrease the activation energy of surface reaction. Therefore, co-catalysts are important especially for hydrogen, oxygen, or carbon monoxide formation in water splitting or CO_2 fixation as artificial photosynthesis.

5. Summary

In this paper, various researches of the charge separation in heterogeneous photocatalysts have been reviewed. In order to develop a highly active photocatalyst, it is necessary to efficiently separate photogenerated charges and suppress the annihilation due to the charge recombination. The charge separation is promoted along the electric field in the crystal for dielectrics and pyroelectric materials with polarized electric fields inside the crystal. To suppress the charge recombination, it is also effective to expose a well-developed crystal facets. Since the electronic states of the semiconductor surface varies depending on the atomic arrangements and the adsorption properties of the crystal planes, the photogenerated charges are separated between different crystal facets. Furthermore, the formation of heterojunction is an effective method for promoting charge separation. Although charge recombination at the interface should be carefully avoided, the junction of semiconductor-semiconductor or metal complex contributes to improved charge separation efficiency. Co-catalyst loading is a powerful technique for improving photocatalytic activity. Co-catalysts are widely used especially in artificial photosynthesis type photocatalysts, because it works as a catalyst for surface chemical reaction as well as an acceptor for photogenerated electrons and holes.

Heterogeneous photocatalysts have been widely used for various applications and become more important in the future. Especially in the research field of light energy conversion, highly active photocatalysts are intensively studied for solar energy conversion and storage. To solve the global energy issue, it is expected that a new highly efficient photocatalyst will be developed by combining the charge separation technics introduced in this review.

References

(1) K. Page, R. G. Palgrave, I. P. Parkin, M. Wilson, S. L. P. Savin, and A. V. Chadwick, J. Mater. Chem., **17** (2007) 95.
(2) H. A. Foster, I. B. Ditta, S. Varghese, A. Steele, and G. Bellanger, Appl. Microbiol. Biotechnol., **90** (2011) 1847.
(3) H. Zhang, C. Ge, C. Zhu, Y. Li, W. Tian1, D. Cheng, and Z. Pan, Phys. Proc., **25** (2012) 240.
(4) A. Fujishima, T. N. Rao, D. A. Tryk, J. Photochem. Photobio. C **1** (2000) 1.
(5) T. Kamegawa, Y. Shimizu, and H. Yamashita, Adv. Mater. **24** (2012) 3697.
(6) A. Fernández, G. Lassaletta, V. M. Jiménez, A. Justo, A. R. González-Elipe, J.-M. Herrmann, H. Tahiri, and Y. Ait-Ichou, Appl. Catal. B, **7** (1995) 49.
(7) M. N. Chong, B. Jin, C. W. K. Chow, and C. Saint, Water Res. **44** (2010) 2997.
(8) I. McConnell, G. Li, G. W. Brudvig, Chem. Biol., **17** (2010) 434.
(9) Y. Tachibana, L. Vayssieres, and J. R. Durrant, Nat. Photonics, **6** (2012) 511.
(10) Z. Zhang and J. T. Yates, Chem. Rev., **112** (2012) 5520.
(11) A. M. Glass, D. von der Linde and T. J. Negran, Appl. Phys. Lett., **25** (1974) 233.
(12) O. Ambacher, J. Smart, J. R. Shealy, N. G. Weimann, K. Chu, M. Murphy, W. J. Schaff, L. F. Eastman, R. Dimitrov, L. Wittmer, M. Stutzmann, W. Rieger and J. Hilsenbeck, J. Appl. Phys., **85** (1999) 3222.
(13) N. V. Burbure, P. A. Salvador and G. S. Rohrer, J. Am. Ceram. Soc., **89** (2006) 2943.
(14) J. L. Giocondi and G. S. Rohrer, J. Phys. Chem. B, **105** (2001) 8275.
(15) J. L. Giocondi and G. S. Rohrer, Chem. Mater., **13** (2001) 241.
(16) A. Bhardwaj, N. V. Burbure, A. Gamalski and G. S. Rohrer, Chem. Mater., **22** (2010) 3527.
(17) J. L. Giocondi and G. S. Rohrer, Top. Catal., **49** (2008) 18.
(18) K. M. Rabe, C. H. Ahn and J.-M. Triscone, Physics of Ferroelectrics: A Modern Perspective, Springer, 2007.
(19) Y. Inoue, K. Sato, K. Sato and H. Miyama, J. Phys. Chem., **90** (1986) 2809.
(20) P. M. Jones, D. E. Gallardo and S. Dunn, Chem. Mater., **20** (2008) 5901.
(21) S. Dunn, P. M. Jones and D. E. Gallardo, J. Am. Chem. Soc., **129** (2007) 8724.

(22) P. M. Jones and S. Dunn, Nanotechnology, **18** (2007) 185702.
(23) S. Dunn, S. Sharp and S. Burgess, Nanotechnology, **20** (2009) 115604.
(24) P. M. Jones and S. Dunn, J. Phys. D: Appl. Phys., **42** (2009) 065408.
(25) S. V. Kalinin, D. A. Bonnell, T. Alvarez, X. Lei, Z. Hu, J. H. Ferris, Q. Zhang and S. Dunn, Nano Lett., **2** (2002) 589.
(26) J. Chen, H. Lu, H.-J. Liu, Y.-H. Chu, S. Dunn, A. Gruverman and N. Valanoor, Appl. Phys. Lett., **102** (2013) 182904.
(27) A. M. Schultz, Y. Zhang, P. A. Salvador and G. S. Rohrer, ACS Appl. Mater. Interfaces, **3** (2012) 1562.
(28) X. Liu, K. Kitamura, K. Terabe, H. Hatano and N. Ohashi, Appl. Phys. Lett., **91** (2007) 044101.
(29) W. J. Wang, B. B. Huang, X. C. Ma, Z. Y. Wang, X. Y. Qin, X. Y. Zhang, Y. Dai, and M. H. Whangbo, Chem. Eur. J. **19** (2013) 14777.
(30) R. Zhang, Y. Dai, Z. Z. Lou, Z. J. Li, Z. Y. Wang, Y. M. Yang, X. Y. Qin, X. Y. Zhang, and B. B. Huang, CrystEngComm **16** (2014) 4931.
(31) Z. Y. Jiang, Y. Y. Liu, M. M. Li, T. Jing, B. B. Huang, X. Y. Zhang, X. Y. Qin, and Y. Dai, Sci. Rep. **6** (2016) 22727.
(32) J. Li, L. J. Cai, J. Shang, Y. Yu, and L. Z. Zhang, Adv. Mater. **28** (2016) 4059.
(33) J. Li, G. M. Zhan, Y. Yu, and L. Z. Zhang, Nat. Commun. **7** (2016) 11480.
(34) J. Zhang, F. J. Shi, J. Lin, D. F. Chen, J. M. Gao, Z. X. Huang, X. X. Ding, and C. C. Tang, Chem. Mater. **20** (2008) 2937.
(35) M. L. Guan, C. Xiao, J. Zhang, S. J. Fan, R. An, Q. M. Cheng, J. F. Xie, M. Zhou, B. J. Ye, and Y. Xie, J. Am. Chem. Soc. **135** (2013) 10411.
(36) X. F. Chang, J. Huang, C. Cheng, Q. Sui, W. Sha, G. B. Ji, S. B. Deng, and G. Yu, Catal. Commun. **11** (2010) 460.
(37) Z. Z. Lou, B. B. Huang, Z. Y. Wang, X. C. Ma, R. Zhang, X. Y. Zhang, X. Y. Qin, Y. Dai, and M. H. Whangbo, Chem. Mater. **26** (2014) 3873.
(38) X. L. Zhu, Z. Y. Wang, B. B. Huang, W. Wei, Y. Dai, X. Y. Zhang, and X. Y. Qin, APL Mater. **3** (2015) 104413.
(39) A. Al-keisy, L. Ren, D. D. Cui, Z. F. Xu, X. Xu, X. D. Su, W. C. Hao, S. X. Dou, Y. and Du, J. Mater. Chem. A **4** (2016) 10992.
(40) X. L. Zhu, P. Wang, B. B. Huang, X. C. Ma, X. Y. Qin, X. Y. Zhang, and Y. Dai, Appl. Catal. B **199** (2016) 315. (19) W. J. Wang, B. B. Huang, X. C. Ma, Z. Y. Wang, X. Y. Qin, X. Y. Zhang, Y. Dai, and M. H. Whangbo, Chem. Eur. J. **19** (2013) 14777.
(41) R. Li, F. Zhang, D. Wang, J. Yang, M. Li, J. Zhu, X. Zhou, H. Fan, and C. Li, Nat. Commun. **4** (2013) 1432.
(42) L. Ye, J. Liu, L. Tian, T. Peng, and L. Zan, Appl. Catal. B **134–135** (2013) 60.

(43) H. Lin, L. Li, M. Zhao, X. Huang, X. Chen, G. Li, and R. Yu, J. Am. Chem. Soc. **134** (2012) 8328.
(44) T. Ohno, K. Sarukawa, and M. Matsumura, New J. Chem. **26** (2002) 1167.
(45) C. Liu, X. Han, S. Xie, Q. Kuang, X. Wang, M. Jin, Z. Xie, and L. Zheng, Chem. Asian J. 8 (2013) 282.
(46) J. Yu, J. Low, W. Xiao, P. Zhou, and M. Jaroniec, J. Am. Chem. Soc. **136** (2014) 8839.
(47) N. Murakami, Y. Kurihara, T. Tsubota, and T. Ohno, J. Phys. Chem. C **113** (2009) 3062.
(48) P. Zhang, T. Tachikawa, Z. Bian, and Z. Majima, Appl. Catal. B **176–177** (2015) 678.
(49) X. Wang, R. Li, Q. Xu, H. Han, and C. Li, Acta Phys. -Chim. Sin. **29** (2013) 1566.
(50) Z. Zheng, B. Huang, J. Lu, X. Qin, X. Zhang, and Y. Dai, Chem. Eur. J. **17** (2011) 15032.
(51) T. Tachikawa, S. Yamashita, and T. Majima, J. Am. Chem. Soc. **133** (2011) 7197.
(52) P. Li, Y. Zhou, Z. Zhao, Q. Xu, X. Wang, M. Xiao, and Z. Zou, J. Am. Chem. Soc. **137** (2015) 9547.
(53) L. Wang, J. Ge, A. Wang, M. Deng, X. Wang, S. Bai, R. Li, J. Jiang, Q. Zhang, Y. Luo, and Y. Xiong, Angew. Chem. Int. Ed. **53** (2014) 5107.
(54) G. Li, X. Tao, R. Chen, F. Fan, and C. Li, Chem. Eur. J. **21** (2015) 14337.
(55) L. Zhang, J. Shi, M. Liu, D. Jing, and L. Guo, Chem. Commun. **50** (2014) 192.
(56) R. Li, H. Han, F. Zhang, D. Wang, and C. Li, Energy Envion. Sci. **7** (2014) 1369.
(57) T. Liu, X. Zhou, M. Dupuisc, and C. Li, Phys. Chem. Chem. Phys. **17** (2015) 23503.
(58) J. Zhu, F. Fan, R. Chen, H. An, Z. Feng, and C. Li, Angew. Chem. Int. Ed. **54** (2015) 9111.
(59) B. Wang, S. Chen, and L. Guo, Appl. Catal. B **166-167** (2015) 320.
(60) B. Wang, S. Chen, and L. Guo, ChemCatChem **8** (2016) 798.
(61) X. Cai, L. Mao, J. Zhang, M. Zhu, M. Fujitsuka, and T. Majima, J. Mat. Chem. A **5** (2017) 10442.
(62) K. Iizuka, T. Wato, Y. Miseki, K. Saito, and A. Kudo, J. Am. Chem. Soc. **133** (2011) 20863.
(63) Y. Miseki, H. Kato, and A. Kudo, Energy Environ. Sci. **2** (2009) 306.
(64) S. Bai, X. Li, Q. Kong, R. Long, C. Wang, J. Jiang, and Y. Xiong, Adv. Mater. **27** (2015) 3444.
(65) L. Zhang, W. Wang, S. Sun, D. Jiang, and E. Gao, Appl. Catal. B **162** (2015) 470.
(66) Z. Haider, J.-Y. Zheng, and Y.-S. Kang, Phys. Chem. Chem. Phys., **18** (2016) 19595.
(67) B. Wang, M. Liu, Z. H. Zhou, and L. Guo, Adv. Sci. **2** (2015) 1500153.
(68) N. Li, M. Liu, Z. Zhou, J. Zhou, Y. Sun, and L. Guo, Nanoscale **6** (2014) 9695.
(69) S. Na-Phattalung, M. F. Smith, K. Kim, M. H. Du, S. H. Wei, S. B. Zhang, and S. Limpijumnong, Phys. Rev. B: Condens. Matter Mater. Phys. 73 (2006) 125205.
(70) G. Mattioli, F. Filippone, P. Alippi, A. A. Bonapasta, Phys. Rev. B: Condens. Matter Mater. Phys. 78 (2008) 241201.
(71) C. Spreafico and J. VandeVondele, Phys. Chem. Chem. Phys. 16 (2014) 26144.

(72) N. Aiga, Q. Jia, K. Watanabe, A. Kudo, T. Sugimoto, and Y. Matsumoto, J. Phys. Chem. C **117** (2013) 9881.
(73) A. Litke, J. M. Hensen, and J. P. Hofmann, J. Phys. Chem. C **121** (2017) 10153.
(74) J. J. M. Vequizo, H. Matsunaga, T. Ishiku, S. Kamimura, T. Ohno, and A. Yamakata, ACS Catal. **7** (2017) 2644.
(75) A. Yamakata, J. J. M. Vequizo, and H. Matsunaga, J. Phys. Chem. C **119** (2015) 24538.
(76) A. Yamakata, H. Yeilin, M. Kawaguchi, T. Hisatomi, J. Kubota, Y. Sakata, and K. Domen, J. Photochem. Photobio. A **313** (2015) 168.
(77) A. Yamakata, J. J. M. Vequizo, and M. Kawaguchi, J. Phys. Chem. C **119** (2015) 1880.
(78) L. B. Hoch, P. Szymanski, K. K. Ghuman, L. He, K. Libao, Q. Qiao, L. M. Reyes, Y. Zhu, M. A. El-Sayed, C. V. Singh, and G. A. Ozin, Proc. Nat. Acad. Sci., **113** (2016) E8011.
(79) J. Xu, Y. Teng, and F. Teng, Sci. Rep. **6** (2016) 32457.
(80) T. H. Jeon, W. Choi, and H. Park, J. Phys. Chem. C **115** (2011) 7134.
(81) K. E. deKrafft, C. Wang, and W. Lin, Adv. Mater. **24** (2012) 2014.
(82) A. J. Cowan, C. J. Barnett, S. R. Pendlebury, M. Barroso, K. Sivula, M. Grätzel, J. R. Durrant, and D. R. Klug, J. Am. Chem. Soc. 133 (2011) 10134.
(83) F. Mou, L. Xu, H. Ma, J. Guan, D. Chen, and S. Wang, Nanoscale **4** (2012) 4650.
(84) S. Rtimi, R. Sanjines, J. Kiwi, C. Pulgarin, M. Bensimon, I. Khmel, and V. Nadtochenko, RSC Adv., **5** (2015) 101751.
(85) S. Rtimi, C. Pulgarin, V. Nadtochenko, F. E. Gostev, I. V. Shelaev, and J. Kiwi, Sci. Rep. **6** (2016) 30113.
(86) Y. Bessekhouad, D. Rober, and J.-V. Weber, Catal. Today **101** (2005) 315.
(87) J. Zhang, H. Zhu, S. Zheng, F. Pan, T. Wang, ACS Appl. Mater. Interfaces **1** (2009) 2111.
(88) L. Yang, S. Luo, Y. Li, Y. Xiao, Q. Kang, and Q. Cai, Environ. Sci. Technol. 44 (2010) 7641.
(89) Y. Wang, Y. Zhang, G. Zhao, H. Tian, H. Shi, and T. Zhou, ACS Appl. Mater. Interfaces 4 (2012) 3965.
(90) M. Law, L. E. Greene, A. Radenovic, T. Kuykendall, J. Liphardt, and P. Yang, J. Phys. Chem. B 110 (2006) 22652.
(91) L. Wu, J. Xing, Y. Hou, F. Y. Xiao, Z. Li, and H. G. Yang, Chem. Eur. J. **19** (2013) 8393.
(92) K. Y. Song, M. K. Park, Y. T. Kwon, H. W. Lee, W. J. Chung, and W. I. Lee, Chem. Mater. **13** (2001) 2349.
(93) F. Ribonia, L. G. Bettini, D. W. Bahnemann, and E. Selli, Catal. Today **209** (2013) 28.
(94) W. Yao, B. Zhang, C. Huang, C. Ma, X. Song, and Q. Xu, J. Mater. Chem. **22** (2012) 4050.
(95) W. Teng, X. Li, Q. Zhao, and G. Chen, J. Mater. Chem. A **1** (2013) 9060.
(96) S. K. Poznyak, D. V. Talapin, and A. I. Kulak, J. Phys. Chem. B **105** (2001) 4816.
(97) D. Shchukin, S. Poznyak, A. Kulak, and P. Pichat, J. Photochem. Photobiol. A **162** (2004)

423.
(98) V. Rodríguez-González, A. Moreno-Rodríguez, M. May, F. Tzompantzi, and R. Gómez, J. Photochem. Photobiol. A **193** (2008) 266.
(99) J. Mu, B. Chen, M. Zhang, Z. Guo, P. Zhang, Z. Zhang, Y. Sun, C. Shao, and Y. Liu, ACS Appl. Mater. Interfaces **4** (2012) 424.
(100) S. Pavasupree, Y. Suzuki, S. Pivsa-Art, and S. Yoshikawa, J. Solid State Chem. 178 (2005) 128.
(101) I. Alessandri, M. Zucca, M. Ferroni, E. Bontempi, and L. E. Depero, Small 5 (2009) 336.
(102) J. Tian, Y. Sang, Z. Zhao, W. Zhou, D. Wang, X. Kang, H. Liu, J. Wang, S. Chen, H. Cai, and H. Huang, Small **9** (2013) 3864.
(103) Y. Ide, N. Inami, H. Hattori, K. Saito, M. Sohmiya, N. Tsunoji, K. Komaguchi, T. Sano, Y. Bando, D. Golberg, and Y. Sugahara, Angew. Chem. Int. Ed. 55 (2016) 3600.
(104) T. Miyagi, M. Kamei, T. Mitsuhashi, T. Ishigaki, and A. Yamazaki, Chem. Phys. Lett. **390** (2004) 399.
(105) S. Shen, X. Wang, T. Chen, Z. Feng, and C. Li, J. Phys. Chem. C 118 (2014) 12661.
(106) X. Wang, Q. Xu, M. Li, S. Shen, X. Wang, Y. Wang, Z. Feng, J. Shi, H. Han, and C. Li, Angew. Chem. Int. Ed. **51** (2012) 13089.
(107) J. Hou, C. Yang, Z. Wang, W. Zhou, S. Jiao, and H. Zhu, Appl. Catal. B **142-143** (2013) 504.
(108) S. Khanchandani, P. K. Srivastava, S. Kumar, S. Ghosh, and A. K. Ganguli, Inorg. Chem. **53** (2014) 8902.
(109) X.-L. Yin, G.-Y. He, B. Sun, W.-J. Jiang, D.-J. Xue, A.-D. Xia, L.-J. Wan, and J.-S. Hu, Nano Energy **28** (2016) 319.
(110) C. Gao, J. Li, Z. Shan, F. Huang, and H. Shen, Mater. Chem. Phys. **122** (2012) 183.
(111) S. K. Sarkar, J. Y. Kim, D. N. Goldstein, N. R. Neale, K. Zhu, C. M. Elliott, A. J. Frank, S. M. George, J. Phys. Chem. C **114** (2010) 8032.
(112) B. Chai, T. Peng, P. Zeng, and J. Mao, J. Mater. Chem. **21** (2011) 14587.
(113) J. Wang, X. Li, X. Li, J. Zhu, and H. Li, Nanoscale **5** (2013) 1876.
(114) G. Tian, Y. Chen, H.-L. Bao, X. Meng, K. Pan, W. Zhou, C. Tian, J.-Q. Wang, and H. Fu, J. Mater. Chem. **22** (2012) 2081.
(115) X. Wang, Y. Tang, Z. Chen, and T.-T. Lim, J. Mater. Chem. **22** (2012) 23149.
(116) Y. Hou, X. Li, Q. Zhao, X. Quan, and G. Chen, J. Mater. Chem. **21** (2011) 18067.
(117) K. K. Nanda, S. Swain, B. Satpati, L. Besra, B. Mishra, and Y. S. Chaudhary, ACS Appl. Mater. Interfaces **7** (2015) 7970.
(118) Z. Zhang, W. Wang, and E. Gao, J. Mater. Sci. **49** (2014) 7325.
(119) E. Borgarello, J. Kiwi, E. Pelizzetti, M. Visca, and M. Grätzel, Nature **289** (1981) 158.
(120) K. Hirano, E. Suzuki, A. Ishikawa, T. Moroi, H. Shiroishi, and M. Kaneko, J. Photochem.

Photobiol. A **136** (2000) 157.
(121) K. Vinodgopal, X. Hua, R. L. Dahlgren, A. G. Lappin, L. K. Patterson, and P. V. Kamat, J. Phys. Chem., **99** (1995)10883.
(122) Y. Saito, W. Kubo, T. Kitamura, Y. Wada, and S. Yanagida, J. Photochem. Photobiol. A **90** (1995) 153.
(123) W. Kim, T. Tachikawa, T. Majima, C. Li, H.-J. Kim and W. Choi, Energy Environ. Sci., **3** (2010) 1789.
(124) M. Zhu, Y. Lu, Y. Du, J. Li, X. Wang, and P. Yang, Int. J. Hydro. Energy **36** (2011) 4298.
(125) T. Hasobe, H. Sakai, K. Mase, K. Ohkubo, and S. Fukuzumi, J. Phys. Chem. C **117** (2013) 4441.
(126) E. Bae, W. Choi, J. Park, H. S. Shin, S. B. Kim, and J. S. Lee, J. Phys. Chem. B **108** (2004) 14093.
(127) E. Bae, and W. Choi, J. Phys. Chem. B **110** (2006) 14792.
(128) K. E. Lee, M. A. Gomez, S. Elouatik, and G. P. Demopoulos, Langmuir **26** (2010) 9575.
(129) H. Hagiwara, N. Ono, T. Inoue, H. Matsumoto, and T. Ishihara, Angew. Chem. Int. Ed. **45** (2006) 1420.
(130) H. Hagiwara, T. Inoue, K. Kaneko, and T. Ishihara, Chem. Eur. J. **15** (2009) 12862.
(131) H. Hagiwara, T. Inoue, S. Ida, and T. Ishihara, Phys. Chem. Chem. Phys., 13 (2011) 18031.
(132) K. Sekizawa, K. Maeda, K. Domen, K. Koike, and O. Ishitani, J. Am. Chem. Soc. **135** (2013) 4596.
(133) S. Sakthivel, M. V. Shankar, M. Palanichamy, B. Arabindoo, D. W. Bahnemann, and V. Murugesan, Water Res. **38** (2004) 3001.
(134) A. A. Ismail, S. A. Al-Sayari, and D. W. Bahnemann, Catal. Today **209** (2013) 2.
(135) O. Merka, D. W. Bahnemann, and M. Wark, ChemCatChem **4** (2012) 1819.
(136) X. Zong, H. Yan, G. Wu, G. Ma, F. Wen, L. Wang, and C. Li, J. Am. Chem. Soc. **130** (2008) 7176.
(137) K. Maeda, D. Lu, K. Teramuraxa, and K. Domen, J. Mater. Chem. **18** (2008) 3539.
(138) K. Maeda, T. Ohno, and K. Domen, Chem. Sci. **2** (2011) 1362.
(139) D. Wang, R. Li, J. Zhu, J. Shi, J. Han, X. Zong, and C. Li, J. Phys. Chem. C **116** (2012) 5082.
(140) M. W. Kanan, and D. G. Nocera, Science **321** (2008) 1072.
(141) C. Ding, J. Shi, D. Wang, Z. Wang, N. Wang, G. Liu, F. Xiong, and C. Li, Phys. Chem. Chem. Phys. **15** (2013) 4589.
(142) Y. P. Xie, G. Liu, G. Q. Lu, H.-M. Cheng, Nanoscale **4** (2012) 1267.
(143) A. Yamakata, M. Kawaguchi, N. Nishimura, T. Minegishi, J. Kubota, and K. Domen, J. Phys. Chem. C **118** (2014) 23897.

富山大学研究推進機構水素同位体科学研究センター研究報告 36：21－29，2016.

論　文

光電子増倍管の印加電圧を制御する改良積分法の液体シンチレーション計測への応用

原　正憲[a]，坂口　春菜[a]，中山　将人[a]，阿蘇　司[b]，庄司　美樹[c]，
古澤　孝良[d]，加藤　結花[d]，吉村　共之[d]

[a]　富山大学　研究推進機構　水素同位体科学研究センター
〒930-8555　富山県富山市五福 3190
[b]　富山高等専門学校　電子情報子工学科
〒939-0293　射水市海老江練合　1-2
[c]　富山大学　研究推進機構　研究推進総合支援センター　生命科学先端研究支援ユニット
〒930-0194　富山市杉谷 2630
[d]　日立製作所
〒181-8622　東京都三鷹市牟礼　6-22-1

Modified integral counting method by controlling high voltage of photomultipliers for liquid scintillation counting

Masanori Hara[a], Haruna Sakaguchi[a], Masato Nakayama[a], Tsukasa Aso[b], Miki Shoji[c], Takayoshi Furusawa[d], Yuka Kato[d], Tomoyuki Yoshimura[d]

[a] Hydrogen Isotope Research Renter, Organization for Promotion of Research, University of Toyama, Gofuku 3190, Toyama 930-8555, Japan
[b] Electronics and Computer Engineering, Toyama National College of Technology, Ebie-neriya 1-2, Imizu city, Toyama 933-0293, Japan
[c] Life Science Research Center, Organization for Promotion of Research, University of Toyama, Sugitani 2630, Toyama 930-0194, Japan
[d] Hitachi, Ltd., 6-22-1 Mure, Mitaka city, Tokyo 181-8622, Japan

(Received January 27, 2017; accepted July 24, 2017)

Abstract

The modified integral counting method by control of the high voltage of photomultipliers (MICM-HV) was investigated to show its applicability for radioactivity analysis. In the MICM-HV, pulse height spectra of the sample are measured at various high voltages of photomultipliers in the liquid scintillation counter. The spectra are converted to integral spectra, which are extrapolated to give the convergence point. The counting rate at the convergence point corresponds to the disintegration rate of the sample. The MICM-HV determines the disintegration rate with one cocktail sample and the method requires no unquenched standard sample.

Keywords: Modified integral counting method, high voltage, photomultiplier, scintillator

1. **Introduction**

Liquid scintillation counting (LSC) is widely used for the radioactivity analysis of beta emitters, whereas LSC requires a quenching correction to determine a counting efficiency. Several quenching correction methods have been proposed. The quenching correction is usually carried out using a quench correction curve which is made by a quenched standard set [1]. Quenched standard sets for both ^{3}H and ^{14}C can be purchased from some suppliers, whereas standards sets for other nuclides need to be prepared by oneself. On the other hand, no quenched standard is required in direct methods [1] such as the integral counting method [2] and the efficiency tracing method [3]. Homma et al. have proposed the modified integral counting method (MICM) [4, 5]. The MICM has been used routine works of moderate precision, because no complicated procedure is necessary. In this method, the disintegration rate is obtained from the integral count rate of the sample at the zero detection threshold (ZDT). However, ^{3}H unquenched standard sample which the activity of ^{3}H is known is required to determine the ZDT. The pulse height spectrum of ^{3}H unquenched sample is measured, and the spectrum obtained is transformed to the integral spectrum,

$$IC(Chi) = \sum_{Ch=Chi}^{Ch_{max}} C(Ch) \qquad (1)$$

where $IC(Chi)$ is the integral counts from a given integral channel (Chi) to the maximum channel (Ch_{max}) and $C(Ch)$ is the count rate at a given channel number, respectively. The integral spectrum is extrapolated to the disintegration rate of the standard sample and the ZDT is found. Subsequently, the pulse height spectrum of an unknown sample is measured and it is converted to the integral spectrum by Eq. (1). The integral spectrum of the sample is extrapolated to the ZDT, the disintegration rate of unknown sample is determined the count rate at the ZDT. To know the disintegration rate of unknown sample the MICM requires an unquenched standard of ^{3}H. The MICM with various quenched samples (MICM-VQ) requires several quenched samples having same amount of radioactive material[6]. In the MICM-VQ these spectra are converted to integral spectra by Eq. (1) and these integral spectra are extrapolated to find the convergence point which corresponds to the ZDT, because the integral counts at the ZDT does not depends on the quenching of the sample. The integral count rate at the ZDT corresponds to the disintegration rate of sample. However, this technique can not be applied for one sample.

In this study, the determination method of the disintegration rate of one sample cocktail without an unquenched standard was developed. Several integral spectra of one sample were obtained by the control of the high voltage of photomultipliers (PMTs). These spectra were extrapolated to find the ZDT like as the MICM-VQ. The disintegration rate of the sample was obtained from the integral counts at the ZDT. The method developed was named as the modified integral counting method by the control of high voltage of PMTs (MICM-HV). The disintegration rates obtained by the MICM-HV were compared with those by the MICM-VQ.

2. Experimental

The quenched standard set of ^{14}C of toluene based scintillator (denoted as TL set) and that of Ultima Gold (denoted as UG set) were purchased as sample cocktails. The quenched standard sets were composed of 10 samples which contained same amount of radioactive material. The disintegration rate of TL set and of UG set were determined to be 128700 dpm and 122200 dpm by suppliers, respectively. The

uncertainty of both sets was ±1.3% in 99% confidence level. The five samples of TL set are named from TL A to TL E with increasing quenching, and the samples of UG set are from UG 1 to UG 5.

The pulse height spectra from scintillation cocktails were measured by the liquid scintillation counter, Aloka LSC-LB5. This scintillation counter has three of PMTs for the scintillation counting with the coincidence unit to reduce the background counts. This system is equipped the 4000 channel multichannel analyzer to register the pulse height spectrum of scintillation cocktail. The channel range for measuring the ^{14}C spectrum was adjusted from 0 to 200 keV. The pulse height spectra of samples were registered for 10 min when the high voltage of PMTs was controlled in the range from 1500 V to 1540 V.

3. Results and discussion

3.1. MICM with various quenched samples

Nakayama et al. reports MICM-VQ can be applied for various liquid scintillators such as toluene and Ultima Gold [7]. The disintegration rates of TL and UG sets were determined by the MICM-VQ. Fig. 1 shows the pulse height spectra of UG set at 1533 V for PMTs. The abscissa and the ordinate are the channel number and the counting rate, respectively. The pulse height of UG 1 with the lowest quenching level is extended to 2500 channel. However, the pulse height of quenched samples decreased with increasing the quenching. On the other hand, the peak positions of pulse height spectra were kept. These spectra were converted to the integral spectra with using

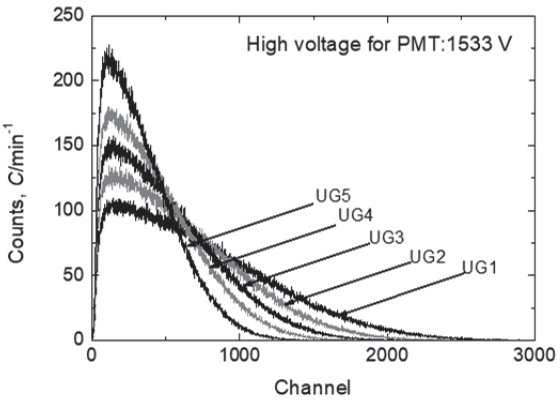

Figure 1. Pulse height spectra of UG set. These spectra were obtained under 1533V of the high voltage of photomultipliers in LSC-LB 5.

Eq. (1). They are shown in Fig. 2. The value of *IC* decreased with increasing *Chi*. The fitting function was obtained from the integral spectrum where a second order function was applied. The fitting was done for the higher channel above the peak around 150 channel when the high channel was set to be satisfied $R^2 \geq 0.9997$. The convergence point was found at -13 channel and the disintegration rate of samples was evaluated to be 123.8 ±0.2 kdpm. Since low energy beta particles can generate insufficient number of photons to detect, a channel number of a convergence point has a negative value. The uncertainty of obtained value is the standard deviation of fitting functions at the convergence point. The counting rate at the convergence point agreed with the assayed value of UG set. The evaluations of the disintegration rate of both TL and UG sets at other values of high voltage of PMTs were listed in Table 1 and 2, respectively. The disintegration rate evaluated agreed with the assayed value by the supplier. Within the measurement range the high voltage of PMTs does not influence on the evaluation of the disintegration rate by the MICM-VQ.

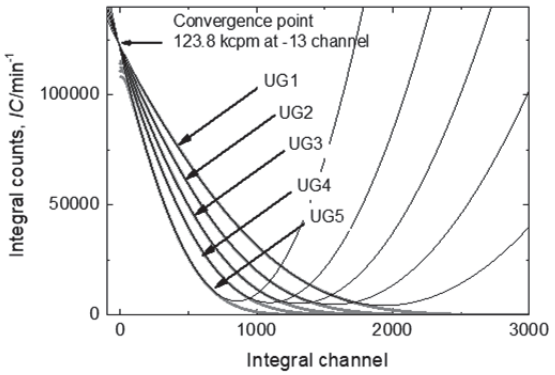

Figure 2. The integral spectra of UG set. The integral spectra were obtained from the pulse height spectra with using Eq. (1). The high voltage of PMTs was adjusted at 1533 V. The bold and thin lines indicate the obtained spectra and the fitting curves, respectively.

Table 1. Obtained value of Toluene quenched set (TL) with MICM-VQ.

High voltage (V)	Convergence point (Chi)	Disintegration rate (kdpm)	[obtained]/[assayed]
1500	-1	128.4±0.3	1.00
1510	-2	128.4±0.4	1.00
1520	-1	128.2±0.4	1.00
1533	-3	128.1±0.3	1.00
1540	1	127.3±0.2	0.99

Table 2. Obtained value of Ultima Gold quenched set (UG) with MICM-VQ.

High voltage (V)	Convergence point (Chi)	Disintegration rate (kdpm)	[obtained]/[assayed]
1500	-15	124.2±0.3	1.02
1510	-13	123.9±0.2	1.01
1520	-13	123.9±0.1	1.01
1533	-13	123.8±0.2	1.01
1540	-12	123.4±0.2	1.01

3.2. MICM by control of high voltage of PMTs

The MICM-VQ requires several samples, which contain same amount of radioactive material, to determine the ZDT. If the several spectra are obtained from one sample, the disintegration rate of its sample will be determined by using the MICM. By controlling the high voltage of PMTs, the pulse height from PMTs can be regulated. The control of high voltages works like an addition of quencher. Therefore, several pulse height spectra can be obtained from one sample by the control of the high voltages. To confirm the applicability of the MICM by the control of the high voltage of PMTs (MICM-HV), the pulse height spectra of both TL and UG sets were obtained under several different values of high voltage.

Fig. 3 shows the dependence of pulse height spectra on the high voltages of PMTs. These spectra were obtained from UG1 which was a less quenched sample in UG set. The pulse height spectra were stretched to the higher pulse height side with increasing high voltage of the PMTs. However, the peak position of the pulse height spectra was maintained around 150

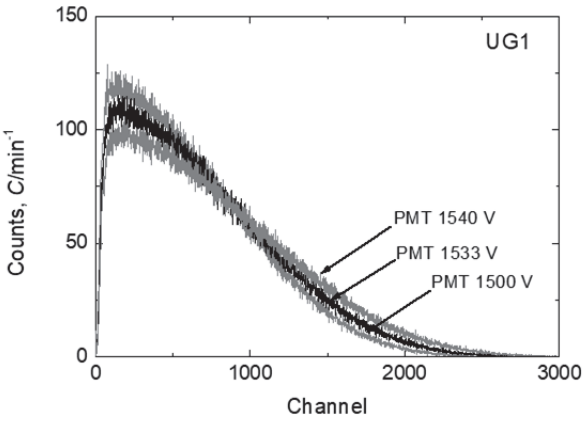

Figure 3. Pulse height spectra of UG 1 at various high voltages of PMTs in LSC-LB5.

channel. This change in the spectra with the variation of high voltages was similar to the effect of the quenching as shown in Fig. 1. In other words, the control of the high voltage of PMTs can provide a set of spectra like a set of quenched samples. These spectra obtained were converted to the integral spectra with using Eq. (1) as shown in Fig. 4. All integral spectra monotonically decreases. These spectra were fitted by a second order function. The fitting curves from the integral spectra obviously show the convergence point at 7 channel. The counting rate at the convergence point was found to be 121.2

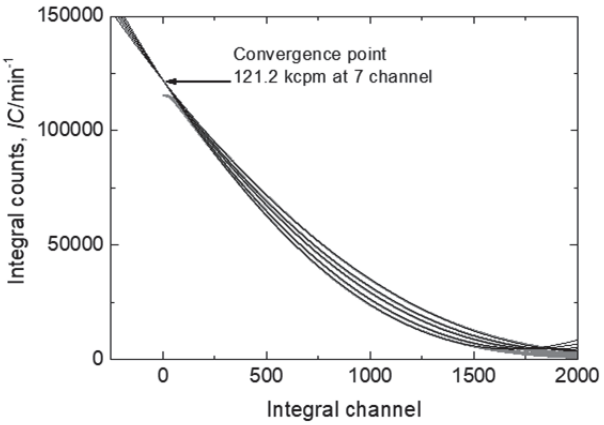

Figure 4. The integral spectra of UG 1 at various high voltages of PMTs. The bold and thin lines indicate the obtained spectra and the fitting curves, respectively.

Table 3. Obtained value of Toluene quenched set with MICM-HV.

Sample	Convergence point (ch.)	Disintegration rate (kdpm)	[obtained]/[assayed]
TL A	35	124.6±0.1	0.97
TL B	35	124.2±0.2	0.97
TL C	30	124.0±0.3	0.96
TL D	21	124.3±0.2	0.97
TL E	9	125.4±0.2	0.97

Table 4. Obtained value of Ultima Gold quenched set with MICM-HV.

Sample	Convergence point (ch.)	Disintegration rate (kdpm)	[obtained]/[assayed]
UG 1	7	121.2±0.1	0.99
UG 2	-23	125.3±0.2	1.03
UG 3	6	120.3±0.2	0.98
UG 4	-9	123.0±0.2	1.01
UG 5	-15	124.3±0.2	1.02

kcpm. The integral spectra of both TL and UG sets were obtained, and the disintegration rates were evaluated from the convergence point. These results of TL and UG were listed in Tables 3 and 4, respectively. In TL set, the disintegration rates evaluated were 3 % less than the assayed value. The values evaluated for UG set slightly deviated from the assayed value within ±3 %. These results indicate that the MICM-HV can be used for the radioactivity measurement of moderate precision. It is also worth to mention that the MICM-HV is able to determine the disintegration rate from only one sample and it was applicable for various scintillators.

4. Conclusions

A new method based on the MICM, MICM-HV, was developed for the measurement of disintegration rate of a single sample without unquenched standard. The pulse height spectra of a sample were measured under various high voltages of PMTs in the commercial liquid scintillation counter. The pulse height spectra obtained were converted to the integral spectra to find the convergence point, and the disintegration rate was determined from the integral counts at the convergence point. The disintegration rate evaluated by the MICM-HV agreed with the assayed value within 3 % of deviation. It indicates that the MICM-HV has a potential for the radioactivity analysis from one sample with moderate precision.

Acknowledgement

This work was supported by JSPS KAKENHI Grant Number 26610065.

References

[1] M.F. L'Annunziata, M. J. Kessler, Liquid scintillation analysis: principles and practice, Chpt. 5, M. F. L'Annunziata (Eds.), Handbook of Radioactivity Analysis. Academic press, California, (2003).

[2] G. Goldstein, Absolute liquid-scintillation counting of beta emitters., Nucleonics

23(1965) 67-69.
[3] M. Takiue, H. Ishikawa, Thermal neutron reaction cross section measurements for fourteen nuclides with a liquid scintillation spectrometer. Nucl. Instrum. Methods., 148(1978) 157-161.
[4] Y. Homma, Y. Murase, K. Hanada, The zero detection threshold of a liquid scintillation spectrometer and its application to liquid scintillation counting, Appl. Radiat. Isot., 45(1994) 341-344.
[5] Y. Homma, Y. Murase, K. Hanada, Absolute liquid scintillation counting of 35S and 45Ca using a modified integral counting method, J. Radioanal. Nucl. Chem., 187(1994) 367-374.
[6] M. Hara, M. Nakayama, K. Hirokami, T. Aso, Appropriate quenching level in modified integral counting method by liquid scintillation counting, J. Radioanal. Nucl. Chem., 310(2016)857-863.
[7] M. Nakayama, M. Hara, M. Matsuyama, K. Hirokami, Modified counting method with various quenched samples for different scintillators, Radio. Safety Manage., 16(2017)1-7.

富山大学研究推進機構水素同位体科学研究センター研究報告 36：31－38，2016.

論　文

Pd–Ag–Rh 三元系合金における磁化率と水素吸収量の相関

赤丸　悟士，原　正憲

富山大学研究推進機構水素同位体科学研究センター
〒930-8555　富山市五福 3190

Relation between the magnetic susceptibility and the amount of absorbed hydrogen for the Pd–Ag–Rh ternary alloy

Satoshi Akamaru, Masanori Hara

Hydrogen Isotope Research Center, Organization for Promotion of Research, University of Toyama
Gofuku 3190, Toyama 930-8555, Japan

(Received January 31, 2017; accepted July 14, 2017)

Abstract

The magnetic susceptibility and equilibrium pressure of a Pd─Ag─Rh ternary alloy and hydrogen system were simultaneously measured, and the relationship between the magnetic susceptibility and the amount of absorbed hydrogen was investigated. The magnetic susceptibility linearly decreased to a value approaching zero with increasing hydrogen content. A high hydrogen content with a magnetic susceptibility close to zero is consistent with a hydride phase. This behavior is similar to that of Pd─Ag or Pd─Rh binary alloys and hydrogen systems, suggesting that the amount of hydrogen absorbed by the Pd─Ag─Rh ternary alloy is correlated with its electronic band structure, as in the case of the Pd-binary alloys.

1. Introduction

Palladium metal is well-known as a hydrogen storage material, and various

applications related to hydrogen usage have been developed including hydrogen sensing and hydrogen purification systems. Pd-based binary alloys that contain a second transition metal have been designed to adjust the hydrogen absorption properties, and systematic studies on Pd-based binary alloys and hydrogen systems have been performed to obtain the relation between the properties and the alloying elements [1].

The amount of hydrogen absorption in metallic Pd depends on its electronic structure; the number of unoccupied d-states is correlated with the amount of absorbed hydrogen [2]. Each absorbed hydrogen atom provides an electron to Pd, thereby occupying the unoccupied d-states of Pd. When the unoccupied d-states of Pd are completely filled with electrons by the absorption of hydrogen, Pd hydride is formed, which cannot undergo further hydrogen absorption.

Alloying Pd with a transition metal is an effective way to control the number of unoccupied d-states in Pd; the amount of absorbed hydrogen is reduced with the supply of electrons from the transition metal to Pd. To determine the relation between the amount of absorbed hydrogen and the unoccupied d-states in a Pd alloy, Pd–Ag, and Pd–Rh were systematically investigated [3]. Because alloying Pd with Ag or Rh corresponds to addition or removal of electrons from Pd, respectively, the number of unoccupied d-states of Pd can be controlled without deformation of the electronic band structure of Pd. Magnetic susceptibility measurements of a Pd alloy with various hydrogen contents can be used to study its electronic structure. The magnetic susceptibility of a Pauli paramagnet is proportional to the density of states at the Fermi level [4]. If the electronic band structure of a Pd alloy is regarded as the same as that of Pd metal, the change in the unoccupied d-states via alloying and the degree of filling of these d-states by hydrogen absorption can be estimated from magnetic susceptibility measurements. We previously investigated the magnetic susceptibility of Pd–Ag and Pd–Rh binary alloys with various hydrogen contents and found that the

amount of absorbed hydrogen was correlated with the amount of doping electron by alloying, namely the amount of substituting elements [3].

The hydrogen absorption properties of Pd-based ternary alloys have not been extensively studied; therefore a lack of the information about the effect of a third element on the hydrogen absorption properties still exists. In the present study, we measured the magnetic susceptibility and the hydrogen absorption isotherm of a Pd–Ag–Rh alloy with various hydrogen contents to verify that the model applied to Pd-based binary alloys can be extended to analyze Pd-based ternary alloys.

2. Experimental

The $Pd_{0.92}Ag_{0.06}Rh_{0.02}$ ternary alloy was used as prepared in previous study [5]. Predetermined amounts of Pd, Ag, and Rh metals were weighed out; then, the mixture was melted in an arc melting furnace [5]. The obtained ingot was grounded into powder using a file, and a part of the powder was subjected to X-ray diffraction (XRD) analysis. Then 1 g of powder was introduced into a quartz cell connected to the pressure–composition isotherm measurement system. The quartz cell was evacuated down to 1.0×10^{-4} Pa; future, the powder alloy was heated at 523 K for 2 h. The magnetic susceptibility of the $Pd_{0.92}Ag_{0.06}Rh_{0.02}$ powder was measured via the induced method, which was described in detail in previous papers [3,6].

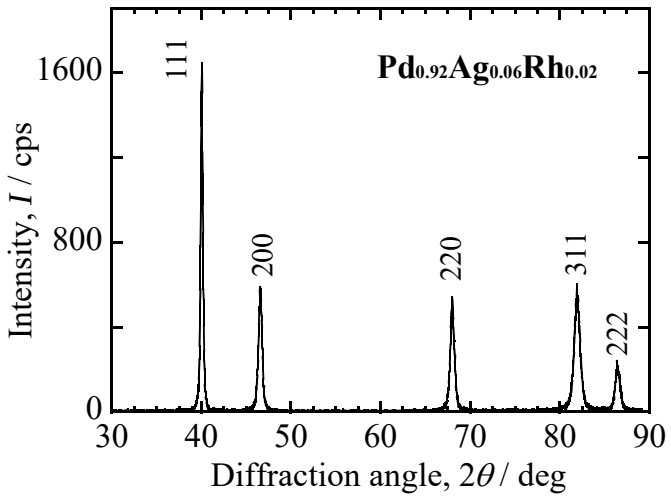

Figure 1 Powder X-ray diffraction pattern of $Pd_{0.92}Ag_{0.06}Rh_{0.02}$ ternary alloy.

3. Results

Figure 1 shows the XRD

pattern of the $Pd_{0.92}Ag_{0.06}Rh_{0.02}$ alloy. The XRD data was indexed using a face-centered cubic structure and no unknown diffraction lines were observed. The lattice constant of the $Pd_{0.92}Ag_{0.06}Rh_{0.02}$ alloy was calculated to be 0.3900 nm. If the $Pd_{0.92}Ag_{0.06}Rh_{0.02}$ ternary alloy was regarded as a binary alloy of $Pd_{0.92}Ag_{0.08}$ and $Pd_{0.92}Rh_{0.08}$, the lattice constant of $Pd_{0.92}Ag_{0.06}Rh_{0.02}$ expected from Vegard's law would have been 0.3898 nm, which was consistent with the measured value. These results indicated that a homogeneous $Pd_{0.92}Ag_{0.06}Rh_{0.02}$ ternary alloy with a face-centered cubic structure was obtained.

Figure 2 shows the dependence of both the magnetic susceptibility and equilibrium pressure on the hydrogen content of $Pd_{0.92}Ag_{0.06}Rh_{0.02}$ (denoted as [H]/[Pd–Ag–Rh]). The equilibrium pressure sharply increased with increasing [H]/[Pd–Ag–Rh] from zero to 0.04. This range corresponded to that of the dissolved hydrogen region. The equilibrium pressure

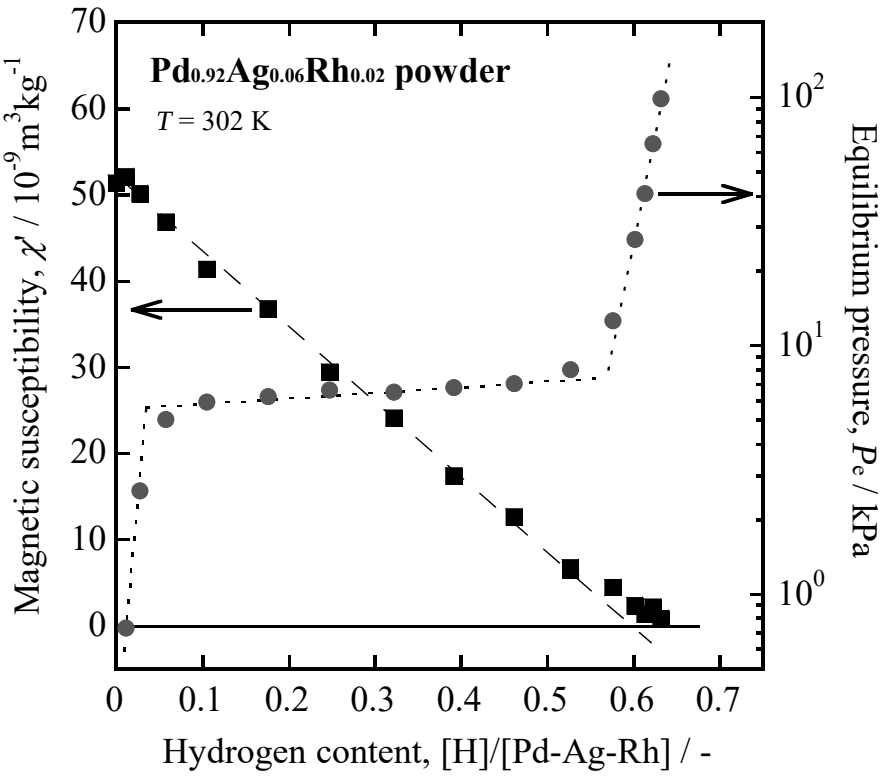

Figure 2 The dependence of both a magnetic susceptibility and an equilibrium pressure on hydrogen content in the $Pd_{0.92}Ag_{0.06}Rh_{0.02}$ ternary alloy. The evaluation of the phase boundary from magnetic susceptibility and equilibrium pressure was performed using the dashed and dotted lines.

was maintained between 6 to7 kPa within 0.1 < [H]/[Pd–Ag–Rh] < 0.5, which is generally called a plateau. Because the equilibrium pressure sharply increased above this value, the hydride phase appeared at [H]/[Pd–Ag–Rh] > 0.6. This behavior was qualitatively the same as that of Pd-based binary alloys and Pd metal [3,6,7].

The magnetic susceptibility of $Pd_{0.92}Ag_{0.06}Rh_{0.02}$ was 51 × 10^{-9} m^3/kg. This value is slightly smaller than that of Pd metal. With increasing [H]/[Pd–Ag–Rh], the magnetic susceptibility linearly decreased to the small positive value of 2 × 10^{-9} m^3/kg at [H]/[Pd–Ag–Rh] > 0.6. The dependence of the magnetic susceptibility on [H]/[Pd–Ag–Rh] was similar to that found for Pd-based binary alloys and Pd metal [3,6,7].

4. Discussion

Since Pd–Ag and Pd–Rh alloys were found to show paramagnetic behavior [3], and the magnetic susceptibility of Pd–Ag–Rh was very small in comparison with that of other Pd-based ferromagnetic binary alloys such as Pd–Co and Pd–Ni [8,9], the $Pd_{0.92}Ag_{0.06}Rh_{0.02}$ alloy is considered to be a paramagnet at room temperature. In addition, we proved in a previous study [3] that the rigid band model could be applied to Pd–Ag and Pd–Rh systems; the electronic band structure of Pd metal was not affect by the substituting Ag or Rh, and the density of states at the Fermi level for Pd-binary alloys was related only to the change in the number of electrons by alloying. Considering that the Ag and Rh content of the Pd ternary alloy used in this study was low, the rigid band model could be applied to the $Pd_{0.92}Ag_{0.06}Rh_{0.02}$ and hydrogen system. In this section, the magnetic susceptibility of the Pd ternary alloy will be analyzed based on the rigid band model.

The principal values obtained from Fig.1 and 2 are summarized in Table 1. The values for Pd metal and Pd-binary alloys are also included for comparison. As cn be extracted from the data, the magnetic susceptibility of $Pd_{0.92}Ag_{0.06}Rh_{0.02}$ without hydrogen is consistent

Table 1. The principal values obtained from Fig.1 and Fig.2. The values for related materials are also summarized in comparison.

	[H]/[Pd–Ag–Rh] at β_{min}		χ' without hydrogen	Plateau pressure	Lattice constant	Ref.
	from P_e	from χ'	/10^{-9}m^{3}kg^{-1}	/kPa	/nm	
$Pd_{0.92}Ag_{0.08}$	0.52	0.49	42.2	0.639	0.3903	[1]
$Pd_{0.96}Ag_{0.04}$	0.57	0.55	50.6	1.04	0.3896	[1]
Pd	0.62	0.63	64.3	2.45	0.3890	[1]
$Pd_{0.96}Rh_{0.04}$	0.67	0.65	73.9	10.3	0.3886	[1]
$Pd_{0.92}Rh_{0.08}$	0.70	0.71 1)	71.1	27.4	0.3883	[1]
$Pd_{0.92}Ag_{0.06}Rh_{0.02}$	0.57	0.60 1)	51.3	6.29	0.3900	This work

1) the value was obtained by the extrapolation of the magnetic susceptibility at the plateau region.

with that of the $Pd_{0.96}Ag_{0.04}$ alloy. Because the magnetic susceptibility of a Pauli paramagnet is proportional to the density of states at the Fermi level [4], this result suggests that the density of states at the Fermi level in $Pd_{0.92}Ag_{0.06}Rh_{0.02}$ is similar to that in $Pd_{0.96}Ag_{0.04}$, and that the number of electrons in both specimens are practically the same.

In the Pd–Ag or Pd–Rh and hydrogen systems, the change in the number of electrons induced by Ag or Rh substitution resulted in the change of the terminal of the plateau because the amount of unoccupied d-states in the absence of hydrogen was related to the minimum hydrogen content at the hydride phase (β_{min}) [3]. The β_{min} for $Pd_{0.92}Ag_{0.06}Rh_{0.02}$ was estimated from the equilibrium pressure; the hydrogen content at the terminal of the plateau was determined at the point where the plateau intersected the extrapolated line of the hydride phase. The obtained value was the same as that for $Pd_{0.96}Ag_{0.04}$, suggesting that the β_{min} for the $Pd_{0.92}Ag_{0.06}Rh_{0.02}$ ternary alloy had the same implications as in the Pd-based binary alloy.

According to our previous study, the magnetic susceptibility of the Pd alloy reached zero at β_{min}, and it kept a small negative value within the hydride phase [3]. Because the

magnetic susceptibility of $Pd_{0.92}Ag_{0.06}Rh_{0.02}$ showed a positive value within the measured [H]/[Pd–Ag–Rh] range, the β_{min} was estimated from the intersection of the extrapolation to zero of the magnetic susceptibility at the plateau region. The estimated value thus obtained was [H]/[Pd–Ag–Rh] = 0.60, which was consistent with the β_{min} estimated from the terminal of the plateau. Consequently, the amount of absorbed hydrogen for the Pd ternary alloy was also correlated with its electronic band structure. It is worth noting that the magnetic susceptibility of the $Pd_{0.92}Ag_{0.06}Rh_{0.02}$ hydride ([H]/[Pd–Ag–Rh] > 0.60) was kept a small positive value, which was indicative of the existence of a small amount of ferromagnetic impurities in the Pd ternary alloy. When the magnetic susceptibility data decreased to 2×10^{-9} m^3/kg, the estimated β_{min} became 0.58, which approached the value obtained from the equilibrium pressure. We tried to estimate the amount of magnetic impurities. As can be extracted from reference [10], the magnetic moments of the constituent atoms in a $Pd_{0.97}Fe_{0.03}$ alloy were determined to be $3.0\mu_B$ for Fe and $0.15\mu_B$ for Pd. The Fe content in the Pd matrix was estimated to be 0.2at% from the enhancement of the magnetization of Pd by a factor of 1.04 induced by the Fe atoms as magnetic impurities. Accordingly, the amount of ferromagnetic impurities could be estimated to be rather small, and the change in the electronic band structure induced by such impurities can be considered negligible in this study.

In the previous study on Pd–Ag and Pd–Rh alloys, the equilibrium pressure at the plateau systematically changed depending on the number of conduction electrons [3]. In the $Pd_{0.92}Ag_{0.06}Rh_{0.02}$ and hydrogen system, however, the equilibrium pressure at the plateau did not follow the same trend [3]. Future investigation on the Pd–Ag–Rh alloy with various element compositions and different hydrogen contents is required to gain a better understanding on this discrepancy.

5. Conclusions

The magnetic susceptibility of a $Pd_{0.92}Ag_{0.06}Rh_{0.02}$ ternary alloy and hydrogen system with various hydrogen contents was measured. It was found that the magnetic susceptibility linearly decreased with increasing the hydrogen content and approached zero at the hydride phase. The hydrogen content at the terminal of the plateau was consistent with that obtained at the point of zero magnetic susceptibility, suggesting that the β_{min} of the Pd–Ag–Rh ternary alloy could be estimated from its magnetic susceptibility measurement, as in the case of the Pd–Ag and Pd–Rh binary alloys.

References

[1] Y. Sakamoto, F. L. Chen, M. Ura, and T. B. Flanagan, *Ber. Bunsenges. Phys. Chem.* 99 (1995) 807-820.
[2] E. Wicke and H. Brodowsky, *Hydrogen in metals II. Application-Oriented properties*, edited by G. Alefeld and J. Völkl (Springer-Verlag, New York, 1978).
[3] S. Akamaru, M. Hara, N. Nunomura, and M. Matsuyama, *Int. J. Hydrogen Energ.* 38 (2013) 7569-7575.
[4] J. M. D. Coey, *Magnetism and Magnetic Materials* (Cambridge University Press, Cambridge, 2010).
[5] H. Fujinami, Bachelor thesis (University of Toyama, 2011).
[6] S. Akamaru, M. Hara, and M. Matsuyama, *J. Alloy. Compd.* 614 (2014) 238-243.
[7] S. Akamaru, M. Hara, and M. Matsuyama, *Rev. Sci. Instru.* 83 (2012) 075102.
[8] S. Akamaru, T. Matsumoto, M. Hara, K. Nishimura, N. Nunomura, and M. Matsuyama, *J. Alloy. Compd.* 580 (2013) S102-S104.
[9] T. Matsumoto, Master thesis (University of Toyama, 2013).
[10] J. W. Cable, E. O. Wollan, and W. C. Koheler, *J. Appl. Phys.* 34 (1963) 1189-1190.

富山大学研究推進機構水素同位体科学研究センター研究報告 36：39－44，2016.

論　文

多角バレルスパッタリング法を用いて調製した Ru–Ni/TiO_2 触媒の CO_2 メタン化反応特性

井上　光浩[1)]、島　明日香[2)]、宮崎　かほり[1)]、専光寺　旭洋[2)]、
オマール　メンドーサ[2)]、魯　保旺[1)]、曽根　理嗣[2)]、阿部　孝之[1)]

1）富山大学研究推進機構水素同位体科学研究センター
〒930-8555　富山市五福 3190
2）宇宙航空研究開発機構
〒168-8522　東京都調布市深大寺東町 7-44-1
〒252-5210　神奈川県相模原市中央区由野台 3-1-1

CO_2 Methanation Performance of a Ru–Ni/TiO_2 Catalyst Prepared by the Polygonal Barrel-Sputtering Method

Mitsuhiro Inoue,[1)] Asuka Shima,[2)] Kaori Miyazaki,[1)] Teruhiro Senkoji,[2)]
Omar Mendoza,[2)] Baowang Lu,[1)] Yoshitsugu Sone,[2)] Takayuki Abe[1)]

1) Hydrogen isotope research center, Organization for promotion of research,
University of Toyama
Gofuku 3190, Toyama 930-8555, Japan
2) Japan Aerospace Exploration Agency,
Jindaiji Higashi-machi 7-44-1, Chofu, Tokyo 182-8522, Japan
Yoshinodai 3-1-1, Chuo-ku, Sagamihara, Kanagawa 252-5210, Japan

(Received April 14, 2017; accepted July 11, 2017)

Abstract

A TiO_2-supported Ru–Ni alloy (Ru–Ni/TiO_2) catalyst (atomic ratio of Ru:Ni = 50:50) for the CO_2 methanation reaction was prepared by the polygonal barrel-sputtering method. Sputtering was performed with an area ratio of the Ru and Ni targets of 1:1, Ar gas pressure of 0.8 Pa, and AC power of the radiofrequency power supply of 100 W without heating. As a result, the Ru–Ni alloy nanoparticles were

highly dispersed on the TiO_2 particles used as the support. The particle sizes were distributed between 1 and 5 nm (average size: 2.5 nm), which is similar to the size distribution of a Ru/TiO_2 sample prepared by the same method in our previous study. However, the CO_2 methanation performance of $Ru–Ni/TiO_2$ is not as high as that of the above-mentioned Ru/TiO_2 sample. This might be because of the lower catalytic activity of Ni than Ru.

1. 緒言

近年、地球温暖化に起因する様々な環境問題が世界中で頻発している。その主因として、二酸化炭素（CO_2）が挙げられており、2015 年 12 月には CO_2 排出量削減に関する新たな枠組みとして「パリ協定」が制定された。このことに関し、我が国は「CO_2 に代表される温室効果ガスの排出量を 2030 年までに 2013 年度比で 26%、2050 年には 80%削減する」という目標を掲げ、パリ協定の批准を目指している。これは、これまで目標としていた「低炭素社会」から更に進んだ「脱炭素社会」への転換を示唆している。

上記の背景から、最近、CO_2 排出量削減に関する検討が活発化している。その中でも CO_2 メタン化反応（$CO_2 + 4H_2 \rightarrow CH_4 + 2H_2O$）は CO_2 を原料として天然ガス・都市ガスであるメタン（CH_4）を合成することから、CO_2 排出量の削減に貢献するだけでなく、CO_2 の資源化を可能にする魅力的な反応である。それ故、この反応を利用したシステムが注目されており、例えば、ドイツアウディ社における「Power to gas system」の試験運転や天然ガス田における CO_2 メタン化反応のベンチスケール実証試験が行われている。しかし、これまでに報告されている触媒では 300～400℃程度の反応温度が必要であり[1-5]、加熱による新たな CO_2 排出が問題視されている。

そこで我々は、CO_2 メタン化反応の低温化を目指し、触媒の高性能化を検討した。その結果、触媒調製法として独自に開発したドライの微粒子表面修飾法である「多角バレルスパッタリング法[6-18]」を用いることにより、従来触媒より反応温度を 200℃以上低温化できる Ru 担持 TiO_2（Ru/TiO_2）触媒を見出した[12,13]。この結果から、本触媒を用いれば、工場等で無駄に捨てられている国内総電力消費量の約 1.25 倍に相当する中低温領域の排熱（約 1 kW）の利用が可能となり、CO_2 フリーの CO_2 メタン化システムが期待できる。

一方、上記した高性能触媒において、反応を 100℃程度にまで低温化すれば、お湯や地熱等の利用が可能となる。これは、工場近傍に制限されている本反応の適用範囲を都市部や温泉地域などにも拡大できる可能性を秘める。

この点に関し、Ru/TiO_2 触媒では担持した Ru 粒子サイズの減少とともに反応が低温化することが明らかとなっている[12,13]。つまり、担持金属の粒子径を更に小さくすれば、反応の低温化が期待できる。そこで本研究では担持金属サイズの減少を目指し、Ru より活性が低いが[12]、原子サイズが小さく、且つ、上記した天然ガス田における CO_2 メタン化反応ベンチスケールテストで性能評価が行われている Ni[1,3,4]との合金化を検討するとともに、これを TiO_2 微粒子に担持した $Ru\text{-}Ni/TiO_2$ 触媒を調製し、その特性を評価した。

2. 実験

2.1 試料の調製

試料の調製には、担体として Ru-Ni 合金の調製条件では SiO_2 ガラス板（2.2 × 2.2 cm、および 2.6 × 7.6 cm、松浪ガラス）、触媒調製では TiO_2 微粒子（ST-41、平均粒径：300 nm、石原産業）を用いた。ターゲットには Ru と Ni 板（25 × 100 mm、豊島製作所）を同時に使用し、合金組成が 50:50 at.%になるようにターゲット面積比を調整した。面積比は Ru、あるいは Ni ターゲット（50 × 100 mm、豊島製作所）を用いてガラス板上に調製した試料から求めたスパッタリング速度比を基に決定した。

試料の調製は以下のように行った[10,12,13]。担体を 8 角バレルに投入し、真空チャンバー内に導入した。ターゲットは下向きに設置し、ロータリーポンプ、油拡散ポンプを用いてチャンバー内を真空排気した。圧力が 8.0×10^{-4} Pa 以下に達した後、Ar ガス（純度：99.9999%）をチャンバー内に供給し、スパッタリングを行った（加熱なし）。この時、バレルはガラス板を用いた場合は固定、TiO_2 微粒子を用いた場合は振り子動作（振幅：±75°、速度：4.3 rpm）させた。スパッタリング後、N_2 ガス（純度：99.99 %）を真空チャンバーに導入し、大気圧に戻してから試料を取り出した。

2.2 物性評価

試料の合金化は X 線回折（XRD: X’pert、Philips）で評価した（線源: Cu Kα、管電圧、電流: 45 kV、40 mA）。ピーク位置は参照試料として用いた Si 粉末（純度: 99.999%、200 メッシュ、フルウチ化学）の 220 ピーク（2θ = 47.30°）を基準にして求めた[10]。合金組成、および TiO_2 微粒子上に担持した Ru 量は蛍光 X 線分析（XRF: PW2300/00、Philips）で測定し、担持量測定における検量線は Ru 粉末（純度：99.98 %、田中貴金属）を用いて作成した。金属の担持状態は透過電子顕微鏡（TEM: JEM-2100、JEOL）で観察した（加速電圧: 200 kV）。

2.3 触媒性能評価

触媒性能は宇宙航空研究開発機構（JAXA）で行われている手法に従い、固定床流通式により以下のように評価した（Figure 1）[16,17]。調製した Ru-Ni/TiO_2 触媒（1 g）をガラスウール（2 g）に分散させた試料を反応管（内径: 2 cm、触媒層高: 3 cm）に充填した。続いて、純 CO_2 ガス（10 ml/min）と純 H_2 ガス（40 ml/min）を混合したガス（CO_2/H_2 = 1/4 (vol./vol.)）を反応管に導入するとともに、マントルヒーターを用いて所定の温度まで加熱した。反応管出口のガスは生成水をトラップで除去した後、熱伝導度検出器（TCD）を装備したガスク

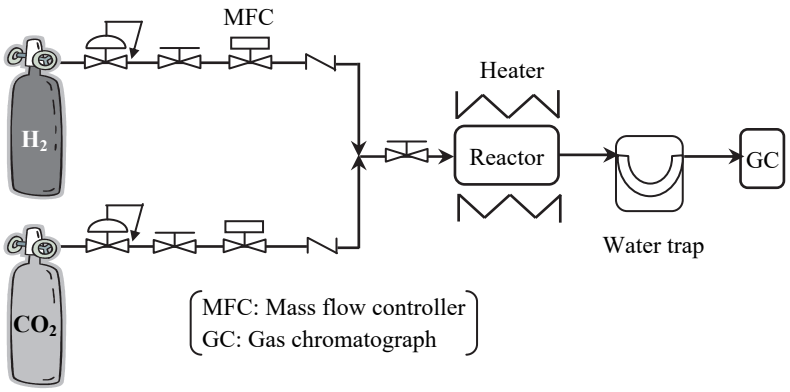

Figure 1 Schematic diagram of CO_2 methanation reactor [16,17].

ロマトグラフ装置（GC-2014、島津製作所）で成分を分析した。この測定では、カラム、およびキャリアガスにShincarbon-ST（信和化工）、Ar ガス（220 kPa で供給）を使用し、ガス注入温度、カラム温度、検出器温度は、いずれも 180℃に設定した。

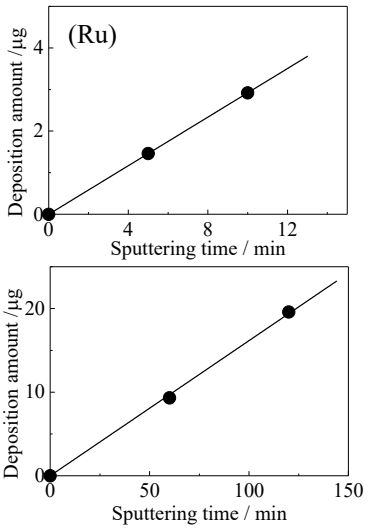

Figure 2 Ru and Ni deposition amounts versus sputtering time.

3. 結果

3.1 スパッタリング条件の検討

50:50 at.%合金調製時のターゲット面積比を検討するために、Ru と Ni のスパッタリング速度を SiO_2 ガラス板を用いて測定した。その結果を Figure 2 に示す（Ar ガス圧: 0.8 Pa、高周波出力: 200 W）。いずれもスパッタリング量と処理時間には直線関係が得られ、傾きからスパッタリング速度は Ru: 0.29 μg/min（2.89 nmol/min）、Ni: 0.16 μg/min（2.85 nmol/min）と求まった。この結果から、ターゲット面積比を 1:1 に決定した。

合金化は、Ar ガス圧: 0.8 Pa、高周波出力: 100 W の条件で検討した。Figure 3(A)は $2\theta = 34$〜$50°$で得られた調製試料（以降、Ru+Ni/glass と表記）の XRD パターンを示す。この図には、Ru、あるいは Ni のみをスパッタリングした試料の結果も載せている（Figure 3(B): Ru/glass、Figure 3(C): Ni/glass）。Ru+Ni/glass には 3 本の回折ピークが $2\theta = 39.20°$、$42.29°$、$44.85°$に認められた。これを六方細密充填構造（HCP）（PDF No 00-006-0663）の Ru/glass、および面心立方格子構造（FCC）（PDF No 00-004-0850）の Ni/glass のパターンと比較すると、形状がブロード化しているとともに配向性の違いによりピーク強度比も変化しているものの、Ru+Ni/glass の結果は Ru/glass に類似する。しかし、ピーク位置は高角度側にシフトし、格子定数（a = 2.588Å、b = 1.494 Å）も Ru の文献値（a = 2.607 Å、b = 1.498 Å）[19]より減少していた。これらは Ru の結晶格子に Ni が溶解し、Ru-Ni 合金が形成されとたことを明示している。なお、XRF 測定から、Ru+Ni/glass の Ru:Ni 比は 43.8:56.2 at.%と求まった。この結果から、上記したスパッタリング条件で 50:50 at.%に近い組成の Ru-Ni 合金が調製できることがわかった。

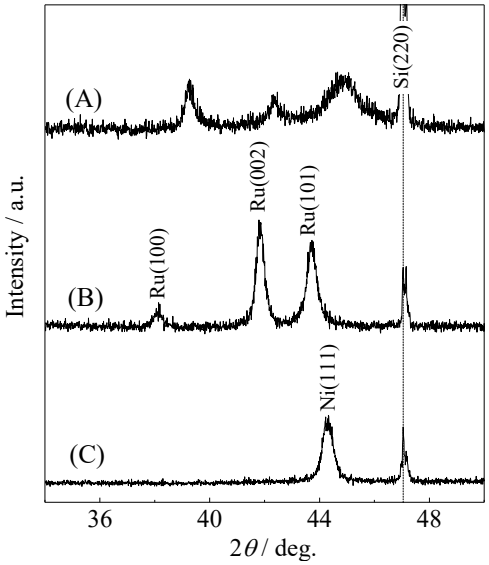

Figure 3 XRD patterns of (A) Ru+Ni/glass, (B) Ru/glass, and (C) Ni/glass (reference peak: Si(220), $2\theta = 47.30°$).

3.2 Ru-Ni/TiO_2 の物性と触媒性能評価

続いて、担体に TiO_2 微粒子を用いて、上記の条件で 40 分間スパッタリングすることにより Ru-Ni/TiO_2 試料を調製した。Figure 4 は調製試料の TEM 像を示す（Ru 担持量: 0.4 wt.%）。灰色の

TiO_2 微粒子上に黒点で表される Ru-Ni ナノ粒子が観測された。粒子サイズは 1〜5 nm に分布し、平均粒径は 2.5 nm と見積もられた（測定粒子数[n] = 97）。上記した粒度分布や平均粒子は、含浸法で調製した Ru/TiO_2 触媒の文献値（粒度分布: 1.4〜29.0 nm、平均粒径: 9.5 nm）[12,13]より、均一、且つ、微細であった。しかし、多角バレルスパッタリング法で調製した Ru/TiO_2 試料（粒度分布: 0.7〜7.5 nm、平均粒径: 2.5 nm）[12,13]と大きな違いはなく、期待していた合金化による担持金属の微細化は認められなかった。

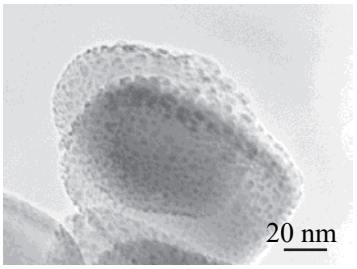

Figure 4 TEM image of the prepared Ru-Ni/TiO_2 sample (Ru deposition amount: 0.4 wt.%).

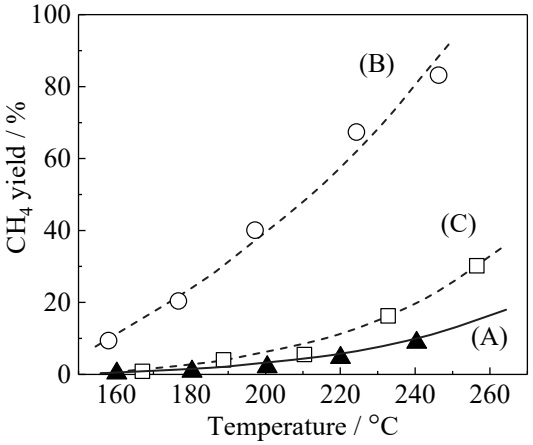

Figure 5 CO_2 methanation performance of (A) Ru-Ni/TiO_2, (B) Ru/TiO_2, and (C) commercial Ru/Al_2O_3 samples ((B) and (C) data were referred from our previous report [16]).

Ru-Ni/TiO_2 の触媒性能は Figure 5(A)に示した。180℃付近からメタン生成が認められ、その収率は 240℃で 8.8%であった。この性能は担持金属の粒径が同等であったにも関わらず、以前報告した Ru/TiO_2（Ru 担持量: 0.8 wt.%、Figure 5(B)）[16]や市販の Ru/Al_2O_3 触媒（Ru 担持量: 0.8 wt.%、NE ケムキャット、Figure 5(C)）[16]より低い。この点に関し、Ni の CO_2 メタン化反応活性は Ru より低いことが明らかにされている[11]。つまり、本研究で調製した Ru-Ni/TiO_2 においては Ni の触媒性能が強く表れ、その結果、CO_2 メタン化反応活性が低下したと考えられる。従って、更に反応を低温化するには合金組成の最適化を検討するとともに、担持金属の微細化に寄与し、且つ、触媒性能を低下させないスパッタリング材料の選定等も行う必要がある。

4. まとめ

本研究では、担持金属の微細化を目指し、Ru より原子サイズの小さい Ni との合金化を検討した。その結果、多角バレルスパッタリング法で調製した Ru-Ni/TiO_2 試料には 1〜5 nm の粒径を持つ合金ナノ粒子が高分散に担持されていた。しかし、この粒径は以前報告した Ru/TiO_2 触媒と同等であり、合金化による粒子サイズの減少効果は認められなかった。なお、触媒性能に関しては Ru/TiO_2 触媒ほど高くなく、この結果は Ni の触媒活性が強く反映されたことに起因すると考えられる。

謝辞

本研究は、JST･CREST の支援を受けたものである（JPMJCR1442）。

References

[1] F.-W. Chang, T.-J. Hsiao, S.-W. Chung and J.-J. Lo, Appl. Catal. A Gen. **164** (1997) 225.

[2] V. Jiménez, P. Sánchez, P. Panagiotopoulou, J. L. Valverde and A. Romero, Appl. Catal. A Gen. **390** (2010) 35.

[3] H. Takano, K. Izumiya, N. Kumagai and K. Hashimoto, Appl. Surf. Sci. 257 (2011) 8171.

[4] S. Tada, T. Shimizu, H. Kameyama, T. Haneda and R. Kikuchi, Int. J. Hydrogen Energy **37** (2012) 5527.

[5] G. Garbarino, D. Bellotti, E. Finocchio, L. Magistri and G. Busca, Catal. Today **277** (2016) 21.

[6] 阿部孝之, 富山大学水素同位体科学研究センター研究報告 **32** (2012) 1.

[7] T. Abe, S. Akamaru and K. Watanabe, J. Alloys Compd. **377** (2004) 194.

[8] T. Abe, S. Higashide, M. Inoue and S. Akamaru, Plasma Chem. Plasma Process **27** (2007) 799.

[9] A. Taguchi, T. Kitami, H. Yamamoto, S. Akamaru, M. Hara and T. Abe, J. Alloys Compd. **441** (2007) 162.

[10] M. Inoue, H. Shingen, T. Kitami, S. Akamaru, A. Taguchi, Y. Kawamoto, A. Tada, K. Ohtawa, K. Ohba, M. Matsuyama, K. Watanabe, I. Tsubone and T. Abe, J. Phys. Chem. C **112** (2008) 1479.

[11] A. Taguchi, M. Inoue, C. Hiromi, M. Tanizawa, T. Kitami and T. Abe, Vacuum 83 (2009) 575.

[12] 谷澤昌昭「平成 20 年度修士論文」

[13] T. Abe, M. Tanizawa, K. Watanabe and A. Taguchi, Energy Environ. Sci. **2** (2009) 315.

[14] C. Hiromi, M. Inoue, A. Taguchi and T. Abe, Electrochim. Acta **56** (2011) 8438.

[15] A. Shima, M. Sakurai, Y. Sone, M. Ohnishi and T. Abe, 42nd International Conference on Environmental Systems (2012) AIAA 2012-3552.

[16] A. Shima, M. Sakurai, Y. Sone, M. Ohnishi, A. Yoneda and T. Abe, Int. J. Microgravity Sci. Appl. **30** (2013) 86.

[17] 島明日香, 桜井誠人, 曽根理嗣, 大西充, 米田晶子, 阿部孝之, 混相流 **27** (2013) 411.

[18] S. Akamaru, T. Shimazaki, M. Kubo and T. Abe, Appl. Catal. A Gen. **470** (2014) 405.

[19] F. Lange, U. Armbruster and A. Martin, Energy Technol. **3** (2012) 55.

富山大学研究推進機構水素同位体科学研究センター研究報告 36：45－52，2016.

ノート

α-Al_2O_3 担持 Pt ナノ粒子触媒の CO 酸化活性と着火現象

田口 明*，尾崎 智弘

富山大学　研究推進機構　水素同位体科学研究センター

〒930-8555　富山市五福 3190

Ignition-extinction phenomena in CO oxidation reaction over “dry” impregnated platinum nanoparticles on α-Al_2O_3

Akira Taguchi*, Tomohiro Ozaki

Hydrogen Isotope Research Center

Organization for Promotion of Research, University of Toyama

Gofuku 3190, Toyama 930-8555

(Received January 31, 2017; accepted July 7, 2017)

Abstract

Catalytic CO oxidation activity of α-Al_2O_3 supported Pt, prepared by the sputter deposition method was investigated. The oxidation activity showed the structure sensitivity with negative particle effects. An ignition-extinction phenomenon was observed in CO oxidation reactions arising from the “mass-transfer limitation” owing to the high turn-over frequency.

Research note

Recent advances in the synthesis and characterization of nanosized particles have promoted an extensive search for methods to prepare highly efficient nanostructured catalysts [1-3]. Sputter deposition, a “dry” impregnation method that does not use any solvent or liquid for catalyst preparation, has gained attention because it has several advantages as compared to the conventional “wet” impregnation method [4-6]. We have investigated the preparation and growth of Pt nanoparticles on Al_2O_3 by FE-SEM and CO chemisorption study [7]. Pt nanoparticles formed in the early stages of sputter deposition were well isolated, and the particle size distribution of Pt nanoparticles was narrow. Longer sputter deposition resulted in growth and coalescence of Pt nanoparticles.

In this note, the catalytic activity of these obtained Pt/Al_2O_3 was studied from the oxidation of CO to CO_2. An intrinsic ignition-extinction phenomena has been observed.

The α-Al_2O_3 supported Pt (Pt/Al_2O_3) used in this study was prepared by a barrel-sputtering system as described in our previous paper [7]. The RF power and Ar gas pressure were 25 W and 0.8 Pa, respectively. Depending on the duration of the sputter deposition, the deposition amount and the diameter of Pt particle obtained were changed. The number of Pt atom on surface, corresponding to the amount of CO adsorbed, and the Pt dispersion calculated from CO chemisorption study were listed in Table 1. Here, the catalysts are denoted as Pt(x), where x represents the Pt dispersion determined by CO chemisorption study [7].

The CO oxidation reaction was studied in a fixed-bed flow reactor (6 mm inner diameter) under atmospheric pressure. Two thermocouples were used, one located in the catalyst in the fixed bed to measure the temperature, and the other on the outside of the quartz reactor to control the reaction temperature via a heater. Reactor effluent gas was analyzed with an on-

Table 1 Preparation, Pt particle diameter and Pt dispersion of Pt/Al_2O_3 [7].

Sample ID	Sputter-deposition time (min)	Pt deposition amount (wt%)	Pt diameter (FE-SEM) (nm)	Pt surface (/g)	Pt dispersion* (-)
Pt(0.70)	4	0.021	1.8	2.18×10^{18}	0.70
Pt(0.50)	5	0.032	2.7	1.57×10^{18}	0.50
Pt(0.31)	7	0.056	3.9	0.95×10^{18}	0.31
Pt(0.25)	9	0.075	4.5	0.77×10^{18}	0.25
Pt(0.18)	20	0.136	5.1	0.57×10^{18}	0.18

* Pt dispersion was investigated at 0 ºC after thermal treatment at 250 ºC under H_2/He flow.

lined gas chromatograph (Shimadzu; GC-8A, column; MS-5A) equipped with TCD. For the reaction test, a mixture of Pt/Al_2O_3 (0.10 g) and unsupported α-Al_2O_3 (2.90 g) as the dilutant was loaded into the reactor. The catalyst was heated to 250 ºC at a ramp rate of 5 ºC/min under He flow. At this temperature, fluid gas was changed to a mixture of H_2 (50 %) and He balance, and this temperature was maintained for additional 1 h. After cooling to room temperature under He flow, the fluid gas was switched to the mixture of CO (0.5%), O_2 (5.0%) and He balance with a total flow rate of 120 ml/min to start the reaction. After 30 min, the effluent gas was analyzed by gas chromatography. The temperature was raised from room temperature to an appropriate one at a ramp rate of 5 ºC/min, and then the effluent gas was analyzed after 30 min. Subsequently, the temperature was raised and catalytic activity was measured in the same manner. This sequence was repeated up to the appropriate temperature where the CO conversion reached 100 %. After reaching 100 % conversion, the temperature was lowered at decrements of 5 ºC until the conversion decreased to a certain value. The CO conversion was calculated from the following equation:

$$\text{Conv.} = \frac{\left([\text{CO}]_{\text{in}} - [\text{CO}]_{\text{out}}\right)}{[\text{CO}]_{\text{in}}} \times 100$$

Here, $[CO]_{in}$ and $[CO]_{out}$ are the concentration of CO in the inflow and the effluent gas,

respectively.

Figure 1 shows the oxidation of CO to CO_2 over Pt(0.70) and Pt(0.25) as a function of temperature. The CO oxidation activity of Pt catalysts was typically low as compared to other transition metals and precious metals [8-10]. Thus, for instance, about 5 % conversion was observed at 165, 170, 180, 190 and 200 ºC for Pt(0.18), Pt(0.25), Pt(0.31), Pt(0.50) and Pt(0.70), respectively. The CO oxidation conversion increased exponentially up to about 60 % with an increase in the reaction temperature, and then the conversion suddenly increased to 100 % with a further increase of 5 ºC in the reaction temperature. This sudden increase of conversion was not due to the lack of the reactant, but rather due to the ignition phenomenon.

The conditions where the conversion reached 100% ($Conv._{100}$) can be predicted using the following relationship:

$$[CO]_{feed} = TOF \times Pt_{surface}$$

Here, $[CO]_{feed}$ represents the number of CO molecules fed in a unit of time (2.6875×10^{17} number/sec). Thus, the expected temperature where the conversion reached 100 % can be calculated from the Arrhenius equation as follows:

$$T = -\left(\frac{E_a}{R}\right)\cdot\left(\frac{1}{\ln(TOF) - \ln(A)}\right)$$

$$= -\left(\frac{E_a}{R}\right)\cdot\left(\frac{1}{\ln\left(\frac{[CO]_{feed}}{Pt_{surface}}\right) - \ln(A)}\right)$$

The temperatures of $Conv._{100}$ for Pt(0.18),

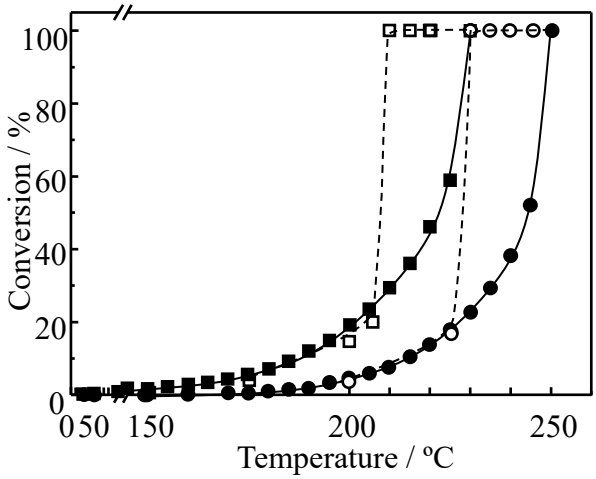

Fig. 1 The conversion of CO to CO_2 as a function of reaction temperature over Pt/Al_2O_3 prepared. (●) Pt(0.70) at rising temperature, (○) Pt(0.70) at lowering temperature, (■) Pt(0.25) at rising temperature, (□) Pt(0.25) at lowering temperature.

Pt(0.25), Pt(0.31), Pt(0.50) and Pt(0.70) were 233.3, 240.5, 242.5, 251.0 and 257.9 ºC, respectively. These values were about 5–10 ºC higher than the empirical ones shown in Figure 1. This fact supports the idea that the sudden increase of conversion was not due to the lack of the reactant, but to the ignition phenomenon.

It should be noted that the catalysis experiments with different amounts of catalyst, i.e., Pt/Al_2O_3 (0.06 g) and CO (0.5 %), O_2 (5%) and He balance with a total flow rate of 80 ml/min, gave almost the same reaction curves as in Figure 1. Thus, it turn out that such an ignition phenomenon arises from the hot spot in the exothermic reaction ($CO + \frac{1}{2}O_2 \rightarrow CO_2$, ΔH = -283.0 kJ/mol). According to the detailed study by Bourane and Bianchi [11-13], the dominant species on a Pt surface change before and after ignition temperature. In that study, although adsorbed CO species were dominant on Pt surface (Pt-CO) before the ignition temperature, strongly adsorbed oxygen species were covered on Pt surface (Pt-O) above the ignition temperature. This was interpreted from the “mass-transfer limitation” owing to the high TOF [12,13].

Lowering the reaction temperature in steps of 5 ºC from the one where 100 % conversion was achieved resulted in the hysteresis in the reaction curve in Figure 1. In Pt(0.70), for example, 100 % conversion was maintained from 250.3 to 230.0 ºC, then suddenly decreased to 17.4 % at 225.3 ºC. A similar hysteresis was observed in other Pt/Al_2O_3 catalysts. The width of hysteresis, defined as the temperature range in which the CO conversion maintained at

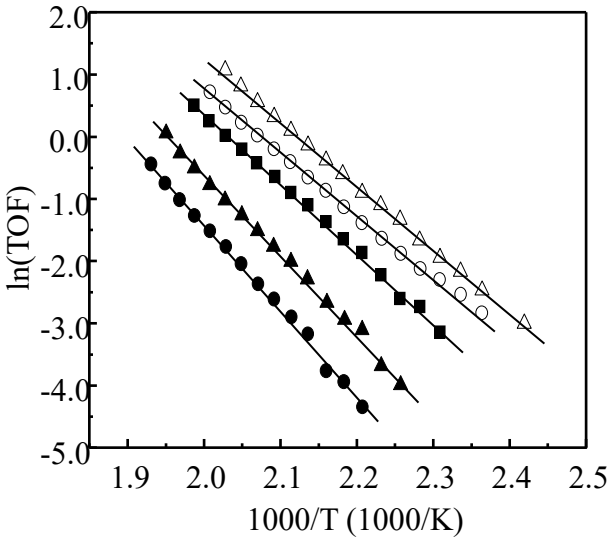

Fig. 2 Arrhenius plot obtained from the oxidation from CO to CO_2 over Pt/Al_2O_3. (●) Pt(0.70), (▲) Pt(0.50), (■) Pt(0.31), (○) Pt(0.25), (Δ) Pt(0.18).

100 %, was about 20–25 ºC and was independent of Pt/Al_2O_3.

Table 2 The Arrhenius parameter at CO oxidation over Pt/Al_2O_3

Sample ID	Activation energy (E_a kJ/mol)	Frequency factor (-)
Pt(0.70)	114.93	2.4857×10^{11}
Pt(0.50)	105.53	5.6359×10^{10}
Pt(0.31)	92.63	6.6465×10^{9}
Pt(0.25)	82.44	8.4260×10^{8}
Pt(0.18)	86.03	3.5210×10^{9}

The Arrhenius plot obtained from TOF, defined as the number of CO_2 molecules formed over each surface Pt atom per second, is shown in Figure 2. The values of E_a and the frequency factor A are listed in Table 2. The E_a was found to decrease with a decrease of Pt dispersion, consistent with previous papers [14,15]. The frequency factor was in the range of 10^{11}–10^{8} s^{-1}, which was in good agreement with previous papers [15-18]. It is clear from Figure 2 that the activity of CO to CO_2 reaction was in the order of Pt(0.18) > Pt(0.25) > Pt(0.31) > Pt(0.50) > Pt(0.70) in the entire temperature region studied. This order indicates a particle size dependence of activity, and this can be clearly seen in Figure 3.

In Figure 3, TOF at 180, 200, and 220 ºC is plotted against the Pt dispersion. Exponential decrease of the activity depending on the Pt dispersion, i.e., the particle diameter of Pt, has been clearly observed [15,19-21], indicating a structure sensitive reaction with negative particle effects according to the classification by Che and Bennett [19]. In addition, Figure 3 reveals that there were two different activities, which became clear when the reaction temperature was raised. They were in low Pt dispersion, corresponding to Pt(0.18), Pt(0.25) and Pt(0.31), and in high Pt dispersion of Pt(0.50) and Pt(0.70). Generating this grouping might give an indication of the effect of agglomeration of Pt nanoparticles. The dispersion dependency in Figure 3 has two possible interpretations: The activity of

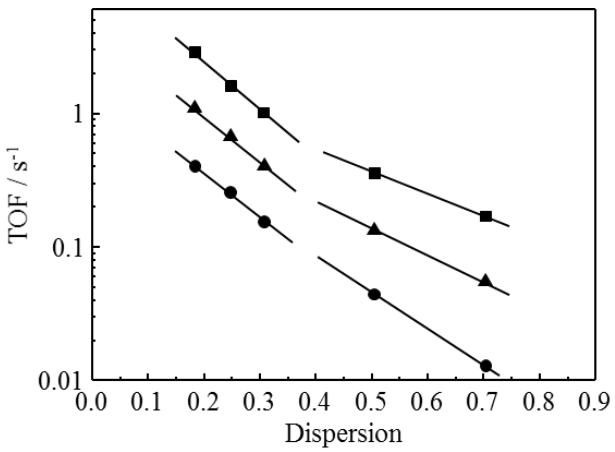

Fig. 3 Relation between TOF and the Pt dispersion of Pt/Al_2O_3. (●) 180 °C, (▲) 200 °C and (■) 220 °C.

Pt with low dispersion was accelerated as compared to the one extrapolated from that of Pt with high dispersion, or, alternatively, the Pt with high dispersion was accelerated as compared to the Pt with low dispersion. An important point is that the value of E_a increased with an increase of the Pt dispersion (Table 2). That is, in Pt with high dispersion, there was a remarkable increase the activity as the reaction temperature increased, resulting in an increase of E_a. Therefore, it can be found that Pt with high dispersion, i.e., small particle diameter, has the potential ability to enhance the CO oxidation activity as compared to the one with low dispersion. Also, it supposes that Pt with high dispersion is suitable for an exothermic reaction such as hydrogen combustion under mild conditions.

In conclusion, CO oxidation activity of α-Al_2O_3 supported Pt catalyst, prepared by a dry impregnation method was studied. An ignition-extinction phenomenon was observed under O_2 rich conditions of O_2/CO=10. The activation energy decreased with a decrease of Pt dispersion, i.e. an increase of Pt diameter. Further, the catalytic activity increased with a decrease of Pt dispersion, showing a structure sensitivity with negative particle effect. Two different activities were observed in the relation between TOF and the Pt dispersion: the Pt/Al_2O_3 with rather high dispersion exhibited higher TOF than the expected one extrapolated from the low dispersion catalysts. This indicates that Pt nanoparticles with small particle diameter possess a potential ability to enhance CO oxidation activity.

References

[1] J. Shen, N. Semagina, ACS Catal. 4 (2014) 268.
[2] B. L. Cushing, V. L. Kolesnichenko, C. J. O'Connor, Chem. Rev. 104 (2004) 3893.
[3] Y. Xia, Y. Xiong, B. Lim, S. E. Skrabalak, Angew. Chem. Int. Ed. 48 (2009) 60.
[4] M. Inoue, H. Shingen, T. Kitami, S. Akamaru, A. Taguchi, Y. Kawamoto, A. Tada, K. Ohtawa, K. Ohba, M. Matsuyama, K. Watanabe, I. Tsubone, T. Abe, J. Phys. Chem. C 112 (2008) 1479.
[5] T. Abe, M. Tanizawa, K. Watanabe, A. Taguchi, Ener. Environment. Sci. 2 (2009) 315.
[6] A. Taguchi, M. Inoue, C. Hiromi, M. Tanizawa, T. Kitami, T. Abe, Vacuum 83 (2009) 575.

[7] A. Taguchi, T. Ozaki, Annual Report of Hydrogen Isotope Research Center, Univ. Toyama 35 (2015) 13.
[8] I. H. Son, M. Shamsuzzoha, A. M. Lane, J. Catal. 210 (2002) 460.
[9] Y. -F. Han, M. J. Kahlich, M. Kinne, R. J. Behm, Appl. Catal. B: Environ. 50 (2004) 209.
[10] P. J. Berlowitz, C. H. F. Peden, D. Wayne Goodman, J. Phys. Chem. 92 (1988) 5213.
[11] A. Bourane, D. Bianchi, J. Catal. 222 (2004) 499.
[12] K. Arnby, A. Törncrona, B. Andersson, M. Skoglundh, J. Catal. 221 (2004) 252.
[13] A. Wille, E. Fridell, Appl. Catal. B: Environ. 70 (2007) 294.
[14] G. S. Zafiris, R. J. Gorte, J. Catal. 140 (1993) 418.
[15] F. J. Gracia, L. Bollmann, E. E. Wolf, J. T. Miller, A. J. Kropf, J. Catal. 220 (2003) 382.
[16] A. Bourane, D. Bianchi, J. Catal. 202 (2001) 34.
[17] R. H. Venderbosch, W. Prins, W. P. M. van Swaaij, Chem. Eng. Sci. 53 (1998) 3355.
[18] R. H. Nibbelke, M. A. J. Campman, J. H. B. Hoebink, G. B. Marin, J. Catal. 171 (1997) 358.
[19] M. Che, C. O. Bennett, Adv. Catal. 36 (1989) 55.
[20] B. Atalik, D. Uner, J. Catal. 241 (2006) 268.
[21] A. Bourane, S. Derrouiche, D. Bianchi, J. Catal. 228 (2004) 288.

編集委員　阿部孝之　椚座圭太郎
佐伯淳　鈴木炎
田口明　萩原英久
橋爪隆　波多野雄治
原正憲

富山大学水素同位体科学研究センター研究報告　第36巻

平成29年9月1日　印刷
平成29年9月15日　発行
編集兼発行者
富山大学研究推進機構水素同位体科学研究センター
富山市五福３１９０

印刷所　前田印刷株式会社
富山市黒瀬610－7
電話　076－407－1282

Published by Hydrogen Isotope Research Center, Organization for Promotion of Research,
University of Toyama
Gofuku 3190, Toyama 930-8555, Japan

リサイクル適性Ⓐ
この印刷物は、印刷用の紙へ
リサイクルできます。